coatings

MDPI

Review

NAP-XPS Applications on Solid Oxide Cells Materials: A Short Review

Davide Cademartori [1,2,†] and Luca Vattuone [3,4,*]

[1] Department of Civil, Chemical and Environmental Engineering, University of Genoa (UNIGE-DICCA), Via all'Opera Pia 15, 16145 Genoa, Italy; davide.cademartori@edu.unige.it
[2] HyGrIn Lab, National Renewable Energy Centre of Spain (CENER), Polígono Industrial Rocaforte, Parcela G2-H1, 31400 Sanguesa, Spain
[3] Physics Department (UNIGE—DIFI), University of Genoa, 16146 Genoa, Italy
[4] CNR—IMEM, Genoa Unit, 16146 Genoa, Italy
* Correspondence: luca.vattuone@unige.it
† Current address: HyGrIn Lab, National Renewable Energy Centre of Spain (CENER), Polígono Industrial Rocaforte, Parcela G2-H1, 31400 Sanguesa, Spain.

Abstract

Performance and durability of solid oxide cells are ruled by surface and interface phenomena occurring under operation. Electrode elementary reactions involve adsorption, charge transfer, surface diffusion and incorporation processes that are sensitive to the applied operating conditions and defect concentration. However, key degradation mechanisms such as cation segregation, catalyst deactivation, phase transformations and microstructural evolution originate at/near the electrode surface. Consequently, understanding the surface chemistry of electrode materials is essential for the development of the next generation electrodes. In this frame, Near-Ambient Pressure X-ray Photoelectron Spectroscopy (NAP-XPS) has emerged as a powerful tool to probe chemically active surfaces under more realistic environments, thus correlating surface science and electrochemistry. This review covers the principles of NAP-XPS and its application to solid oxide cell materials, including ceria-based model electrodes, Ni-containing fuel electrodes, exsolved perovskites and mixed ionic-electronic conducting air electrodes. NAP-XPS demonstrated the ability to directly monitor the dynamic state of the electrode surface under controlled operating conditions. Common mechanistic insights and emerging trends are highlighted, together with potential limitations associated with current experimental configurations. Overall, combined NAP-XPS and electrochemical analyses appear to hold the potential for linking surface chemistry with electrode performance and degradation, thus supporting the rational design of the next-generation solid oxide cell materials.

Keywords: NAP-XPS; solid oxide cells; surface processes; fuel electrodes; air electrodes

Academic Editor: Chih-Ming Chen

Received: 26 June 2026
Revised: 15 July 2026
Accepted: 16 July 2026
Published: 20 July 2026

1. Introduction

Within electrochemical devices for energy conversion and storage, reversible Solid Oxide Cells (rSOCs) are progressively gaining momentum thanks to their inherent characteristics, which can provide ease in scalability, long-term discharge and low environmental impact. An rSOC stack is composed of individual cells combined in series and can operate alternatively in fuel cell mode (SOFC), as an *X-to-Power* system, and electrolysis mode (SOEC) as a *Power-to-X system*. Furthermore, rSOC systems hold inherent operational advantages such as:

- Flexibility with regard to the system size and the use of different fuels. rSOC-based systems can theoretically be scaled up or down without showing losses in the thermodynamic performance. The intrinsic modularity of the stacks also offers the opportunity of designing systems of different power sizes. RSOCs are also flexible with respect to the nature of the inlet fuel and can be fed with hydrocarbons or ammonia [1–3].
- The system can be integrated (electrically, thermally or chemically) with renewable energy sources (RES) and different industrial applications [1].
- High efficiency—It is envisaged that EES (Electrical Energy Storage) systems based on rSOCs can achieve up to 70% round-trip efficiency [4].

In light of the aforementioned considerations, rSOCs hold the necessary characteristics to increase RES penetration, improve energy efficiency and facilitate the development of a hydrogen value chain [5]. However, this technology is still waiting for a definitive commercial deployment. Besides financial issues (coming also from the high cost related to cell and stack materials [6,7]), the rSOCs development is slowed down by their technological performance that still requires further improvement from cell to system scale. In particular, the optimization of the electrochemical response at material and cell levels is regarded as one of the keys to increase durability and enable their effective scale-up to systems targeting MW-power size [5]. Many research efforts are still devoted to the optimization of the cell performance by the synthesis of innovative electrocatalysts, adoption of widely available and low-cost materials, development of new manufacturing techniques and cell architectures [8–13].

The state-of-the-art commercial SOCs architecture is the fuel electrode-supported one, featuring a 250–300 μm thick supporting fuel electrode, a 5–15 μm dense electrolyte and a 30–40 μm air electrode. The state-of-the-art fuel electrodes are typically dual-phase systems composed of supporting and active layers, both featuring nickel-yttria stabilized zirconia (Ni-YSZ cermet). The support includes a composite of Ni and $Zr_{0.94}Y_{0.06}O_{1.96}$ (3YSZ) with a relatively coarse structure featuring 30–35 vol% porosity. On the other hand, conventional active fuel electrodes usually contain Ni and $Zr_{0.84}Y_{0.16}O_{1.92}$ (8YSZ) in a 40–60 vol% ratio, featuring finer microstructure and lower porosity to increase the density of reactive sites (i.e., the triple phase boundary length). The full cell support thickness ranges between 250 and 350 μm, with the active layer holding a thickness of 20–30 μm [13]. Both Ni–YSZ cermet layers are prepared and sintered as NiO-YSZ composites, and then NiO is reduced to metallic Ni when exposed to H_2. The electrolyte typically consists of 8YSZ (i.e., a pure ion-conducting material), as this composition has the highest oxide ion conductivity of yttria-doped zirconia. Nonetheless, other materials such as scandia-doped zirconia, gadolinium-doped ceria (GDC) and $La_{0.8}Sr_{0.2}Ga_{0.8}Mg_{0.2}O_{3-\delta}$ (LSGM) have also been investigated for their higher ion transport properties [11–16]. The common materials included in the air electrode show a perovskite structure and, amongst them, $La_{1-x}Sr_xMnO_3$ (LSM) has been one of the most studied for its phase stability at high temperature. However, in its suitable operating temperature range (800–1000 °C), LSM shows high electronic conductivity (200 S/cm at 900 °C) but poor ion-conducting properties ($\approx 10^{-8}$ S/cm). Therefore, LSM is progressively being substituted by other perovskite materials such as $La_{1-x}Sr_xCoO_3$ (LSC) and $La_{1-x}Sr_xFe_{1-y}Co_yO_3$ (LSCF) due to their high electrocatalytic and Mixed Ionic Electronic Conduction (MIEC) properties (with average total conductivities of $\approx 10^2$ S/cm^2) [13–16]. Additionally, several studies reported in the literature are also targeting the use of Co-free air electrodes and the engineering of their performance by microstructural optimization, thus highlighting the increasing effort to identify innovative and sustainable materials for the next generation of SOCs [17–27]. At conventional operating temperatures, state-of-the-art air electrode materials (LSCF and LSC) react with YSZ, forming a resistive phase ($SrZrO_3$), thereby requiring the deposition of

an additional reaction barrier of $Ce_{0.9}Gd_{0.1}O_{1.95}$ (GDC or CGO) between the YSZ electrolyte and the air electrode perovskite [28–30]. Therefore, to improve the adhesion of the air electrode and decrease the Thermal Expansion Coefficient (TEC) mismatch between GDC and the electrocatalyst, a composite GDC-LSC/LSCF is typically used as the air electrode. An SEM micrograph showing the cross-section of a typical cell is shown in Figure 1.

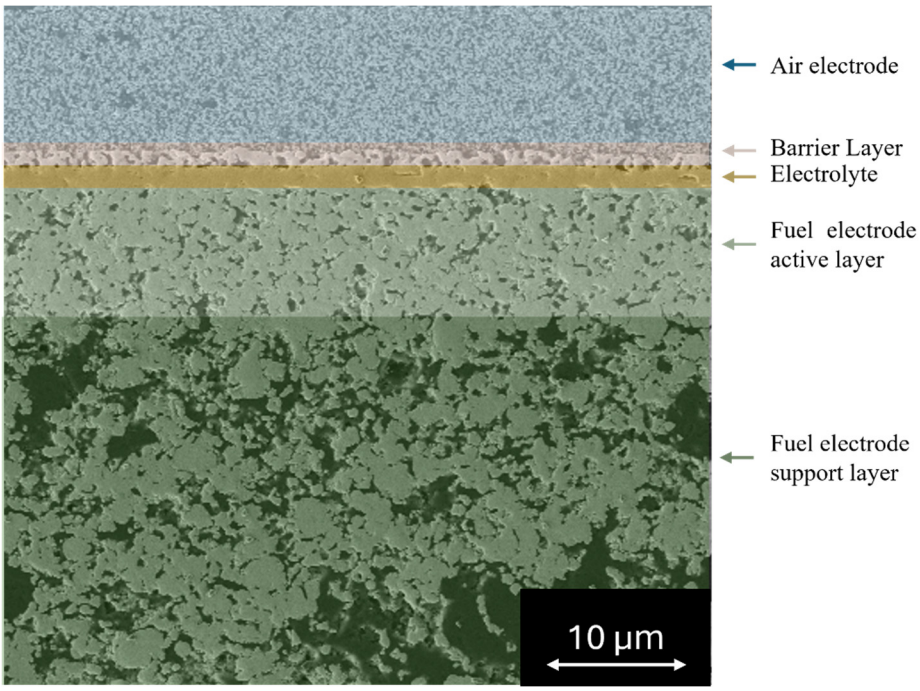

Figure 1. SEM micrograph displaying the morphology of the ceramic layers included in a state-of-the-art fuel electrode-supported solid oxide cell.

2. Impact of Surface-Related Processes in SOCs

Overall, SOCs represent a prime example of multi-layered electrochemical devices, consisting of a dense oxide-ion conducting electrolyte sandwiched between porous composite electrodes, where materials with intrinsic ionic, electronic and catalytic properties are closely coupled across multiple scales. Their inherent architecture makes the electrochemical response not only driven by bulk properties but also by processes occurring at surfaces and interfaces, where gas-phase reactants, ions and electronic charge carriers interact. In conventional composite electrodes, these processes are localized at triple phase boundaries (TPBs) or even up to the entire gas-exposed surface (depending on the electrode materials, gas atmosphere and operating conditions), thus making the role of surface chemistry crucial towards the electrochemical response [31–33]. As an example, in Ni-YSZ fuel electrodes, Ni and YSZ account for the electronic and ionic conductivity and catalytic activity for fuel oxidation/reduction and their microstructural arrangement determines the density and effectiveness of active reaction sites. Similarly, in air electrodes based on perovskite oxides such as LSCF, the electrochemical performance is driven by the interplay between bulk defect chemistry (e.g., oxygen vacancy concentration), surface exchange kinetics and interfacial transport phenomena. Specifically, at a mechanistic level, the electrode reaction pathway can include multiple elementary surface steps such as adsorption of molecular species, dissociation, surface diffusion, charge transfer and lattice incorporation/excorporation. All these steps are governed by local surface composition, defect structure and operating conditions (e.g., temperature, gas composition and electrochemical polarization) [34–37]. Additionally, both activity and long-term stability of SOCs can be controlled by surface-related phenomena. A classic example is represented by the surface

segregation of Sr in LSCF, which leads to the formation of Sr-rich secondary phases (e.g., SrO, carbonates, hydroxides) that block catalytically active sites and suppress the oxygen kinetics [38–40]. Recent studies have shown that this segregation is closely linked to defect chemistry, specifically to the interaction between oxygen vacancies and dopant cations, and can be further enhanced under electrochemical polarization or reactive atmospheres [41]. Alongside cation segregation, additional degradation mechanisms such as Ni coarsening in Ni-YSZ anodes, phase decomposition, and interfacial unwanted reactions (e.g., $SrZrO_3$ formation) contribute to the gradual loss of active surface area and TPB density, finally limiting the durability of SOCs [32,33,42–45].

Recent advances have further underscored that microstructural and surface properties can be actively tuned to enhance performance and durability [19,46–49]. For instance, ad hoc surface modification strategies demonstrated the ability to effectively suppress Sr segregation and enhance oxygen reduction reaction (ORR) kinetics, thereby highlighting the central role of surface defect chemistry in controlling electrochemical activity [38]. From a broader perspective, the growing use of in situ and in operando characterization techniques has highlighted that SOCs electrode surfaces (i) are highly dynamic systems, continuously evolving under realistic operating conditions and (ii) cannot be accurately captured by standalone ex situ characterizations. In this context, Near-Ambient Pressure X-ray Photoelectron Spectroscopy (NAP-XPS) has emerged as an advanced diagnostic tool for investigating and increasing the mechanistic understanding of SOCs-relevant surface processes. The use of NAP-XPS can, indeed, lead to the direct observation of surface composition, oxidation states, adsorbates and reaction intermediates under more realistic operating conditions for SOCs, also potentially probing the occurrence of degradation phenomena such as Sr segregation, surface reconstruction or catalyst deactivation [50,51].

3. NAP-XPS for Electrochemical Energy Applications

NAP-XPS is a relatively modern experimental tool that allows measuring the spectrum of electrons photoemitted by a sample when it is irradiated by X-ray photons in the presence of a gas mixture or a thin liquid layer. Due to the presence of gas or liquid media, the electrons photoemitted by the surface of the sample are scattered or adsorbed, thus limiting the electron flux that can reach the analyzer and be detected. In this frame, the reader is referred to specialized literature for further details and a comprehensive treatment of the existing experimental setups (see, e.g., [52–54], including also microscopic facilities [55] and solid–liquid interfaces [56]). The aim of this section is, indeed, to summarize the main features of the use of NAP-XPS for electrochemical systems relevant to this brief review, ultimately focusing on its specific applications to SOCs.

Experimentally, the X-ray source can be either a conventional (usually monochromatized) laboratory source, such as Al K-alpha or Mg K-alpha or a combination of them (e.g., the recently developed tri-color source [57]), or a synchrotron light source. During the analysis, the photons impinge onto the surface and electrons are photoemitted with different kinetic energies. The spectrum of the photoemitted electrons is obtained by firstly decelerating them to the entrance of a hemispherical deflection analyzer operated at constant pass energy. The analyzer focuses the electrons at its exit slit. These are then accelerated to the detector, which can be either a single channeltron or, more commonly, a multiple channel system; alternatively, a channel-plate is used in more advanced equipment, thus taking advantage of parallel detection which reduces the acquisition time. The spectrum is recorded by scanning the potential of the entrance of the analyzer with respect to the sample. The pass energy of the analyzer then determines the energy resolution.

The photoemission intensity $I_{0\ Xnm}$ under ultra-high vacuum (UHV) can be expressed as:

$$I_{0\ Xnm} \propto \phi_{UHV}(v) \cdot \sigma_{Xnm}(v) \cdot T(hv\ -\ EB_{Xnm})\ n_X \quad (1)$$

where n_X is the number of emitters, X in the region irradiated by the photon beam, $\phi_{UHV}(v)$ is the photon flux at frequency v, $\sigma_{Xnm}(v)$ is the photoemission cross section for an atom X for the level nm (e.g., 1s, 2p, etc.), and $T(hv\ -\ EB_{Xnm})$ is the transmission function of the analyzer for electrons photoemitted with kinetic energy $hv\ -\ EB_{Xnm}$. Due to the slow variation in T with kinetic energy, the correction due to the work function is omitted. In the presence of gases (or liquids) at pressure p, the photon flux $\phi(v)$ arriving at the surface is lower than $\phi_{UHV}(v)$ due to X-ray adsorption. The flux of photoemitted electrons is also scattered, reducing the intensity at the detector. The final intensity $I_{0\ Xnm}$ decreases exponentially with the path for the electrons d_{El} and with the path for X-rays d_X:

$$I_{Xnm} = I_{0\ Xnm}\, e^{-\frac{d_{El}\ \sum\ p}{k\ T}} \propto \phi_{UHV}(v) \cdot e^{-\frac{d_X}{\lambda}} \cdot \sigma_{Xnm}(v) \cdot T(hv\ -\ EB_{Xnm})\ n_X \cdot e^{-\frac{d_{El}\ \sum\ p}{k\ T}} \quad (2)$$

where λ is the mean free path for the photons of energy hv at pressure p in gas Y and $\sum$ the total cross section for electron scattering at kinetic energy $hv\ -\ EB_{Xnm}$.

Within the illustration reported in Figure 2, the red curve displays the O 1s photoelectron excitation cross section as a function of photon energy (right axis, $\sigma_{Xnm}(v)$ in Equation (2)). On the other hand, the four green curves and the blue one indicate the change in the detected intensity I_{Xnm} for p = 1, 5, 10, and 30 mbar of water vapor and for p = 30 mbar of nitrogen gas, respectively, using the same path length for X-rays (d_X = 20 mm) and electrons (d_{El} = 0.3 mm) [54].

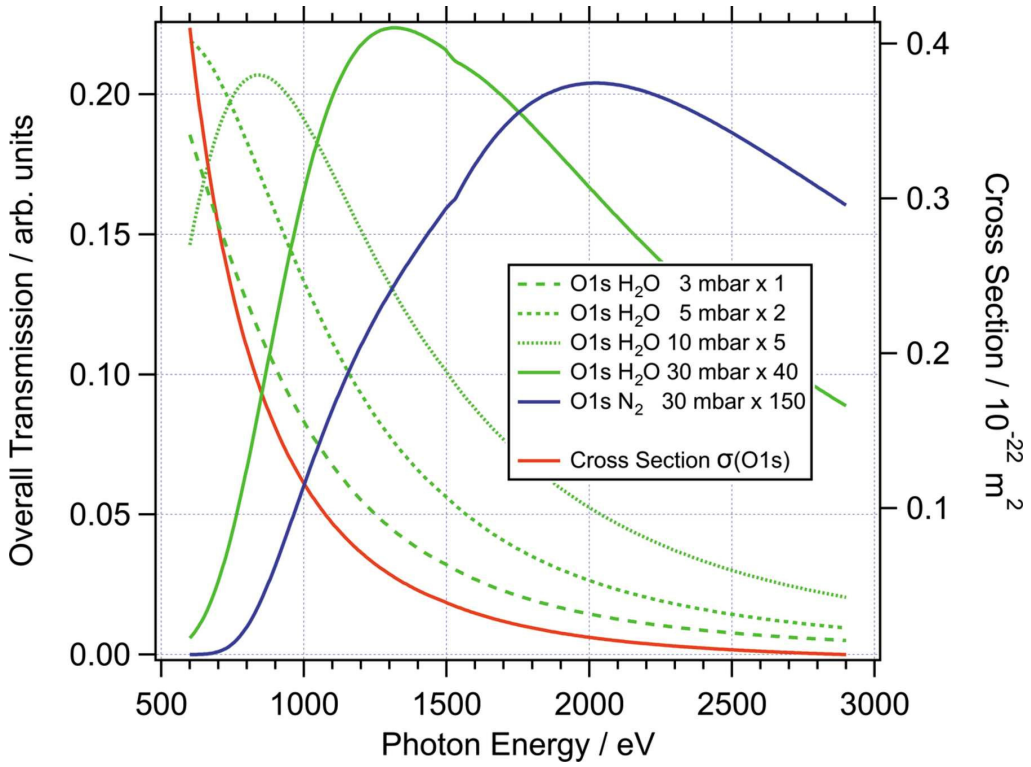

Figure 2. Overall transmission (left scale) for the O 1s line in H_2O vapor at different pressures (green traces) and in N_2 at 30 mbar (blue trace) and O 1s photoemission cross section (red trace, right scale). Note that the data have been multiplied by increasing factors (1 to 150) with increasing pressure. Taken with permission from [54].

In Figure 2, the photon flux is assumed to be constant and the transmission function to be unitary. It would also be necessary to consider that the photon flux depends on photon energy and that the transmission function of the electron analyzer is also not constant. Nonetheless, Figure 2 clearly evidences that the photon energy must be optimized to reach a compromise between the decrease in the photoemission cross section (which would favor lower photon energies) and the increase in electron mean free path (which would favor, on the contrary, higher photon energies).

Most NAP-XPS systems can operate in the mbar range. Due to their high cost, such equipment is still rare but can provide advanced information and increase the understanding of the system under analysis. In this frame, the reader is referred to highly cited reviews for a more complete overview of the results obtained with NAP-XPS for heterogeneous catalysis [58–61], electrochemical reactions [62] and fuel cells [63].

Despite this, in many cases, the operating NAP-XPS pressure is still not high enough to study in operando reactions, which occur with significant rates only in the bar range. Figure 2 displays that the increase in the operating pressure can be attained either by further increasing the photon energy or by reducing the thickness of the gas or liquid layer. To the best of the authors' knowledge, the highest-pressure NAP-XPS system was operated at around 1 bar. Two main approaches have been used to reach this range:

(a) Using harder photons (2.4–15 keV), the kinetic energy of the photoemitted electrons increases, as well as their mean free path [64,65];
(b) Limiting the thickness of the gas layer where the pressure is high to a few tens of microns. This is achieved by using hydrodynamic methods to expose the sample (de Laval nozzle inlet) without increasing the photon energy [66].

Additionally, such high operating pressures can be attained only with dedicated and recently developed experimental setups. These are now more commonly referred to as APXPS (Ambient Pressure XPS) in order to distinguish them from the slightly more widespread NAP-XPS systems, which generally operate in the mbar pressure range.

A typical experimental arrangement is shown in Figure 3a,b, while examples of spectra are displayed in Figure 3c [53].

In the setup used at SILS [53], the working electrode (here Ir(001) single crystal surface) is grounded so that the Fermi levels of the sample and spectrometer coincide. For this reason, the corresponding iridium core level peaks do not shift with the bias applied to the electrolyte. On the contrary, the O 1s core-level peaks associated with the liquid (533.2 eV) and gas-phase water (535.6 eV) shift proportionally by a factor of $\times 0.82$ to the applied bias. The reason the factor is not exactly 1 is related to the limited ionic strength of the solution and the very thin thickness of the electrolyte film. The small shoulder at the low binding energy side of the O 1s spectrum (531 eV at a bias of + 1.05 V) indicates the presence of OH groups in the liquid film. The K 2p spin–orbit doublet overlapping with the Ir $4d^{5/2}$ signal clearly shifts with the applied potential, as potassium is part of the electrolyte. Surprisingly, this is also true for the C 1s signal, thus suggesting that the electrolyte/Ir(001) interface is clean and that the carbon contamination is clearly outside the Helmholtz layer, either within the thin liquid film or at the surface of the liquid.

Another example of the capabilities of NAP-XPS towards the investigation of electrochemical energy devices was provided by its use for probing a battery electrolyte drop. Maibach et al. reported ambient pressure photoelectron spectroscopy data of propylene carbonate in the liquid phase by using solvent vapor as the stabilizing environment [67].

The binding energy scale is calibrated versus the hydrocarbon peak at 285 eV. The APPES spectra of the Solv-Drop sample are shown in the upper part of Figure 4 (top, black spectra). The absence of signal in the Li 1s region proves that (i) the spot is thick enough to sample only the liquid and (ii) Li from the substrate does not dissolve into the solvent.

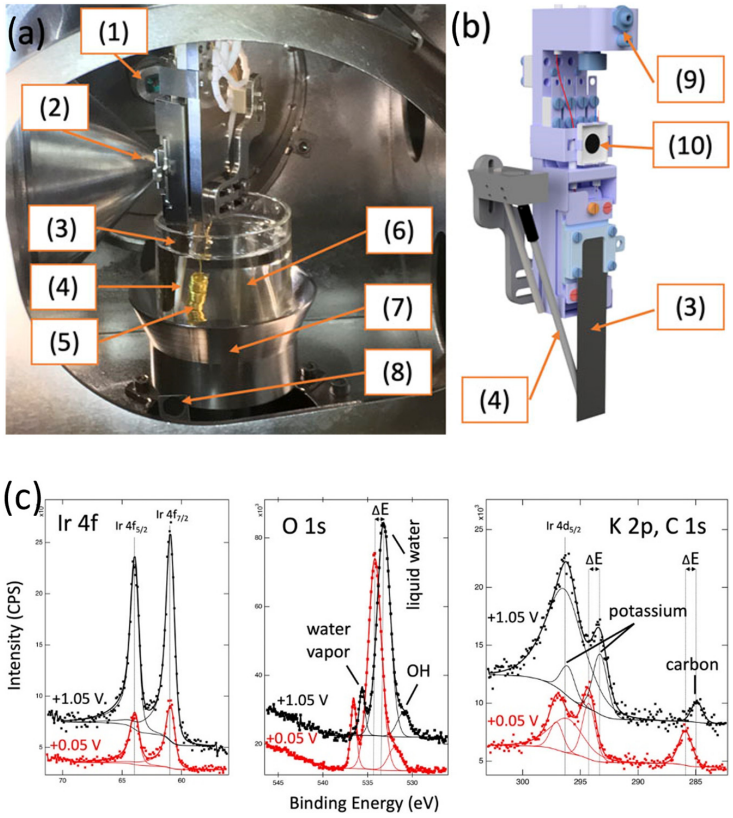

Figure 3. View inside the analysis chamber showing (**a**) a photograph and (**b**) a 3D CAD rendering of the manipulator insert. The relevant components are labeled using numbers: (1) silicon nitride membrane separating the beamline and the APXPS chamber, (2) Ti cone of the electron analyzer, (3) sample (50 × 10 mm^2), configured as a working electrode (WE) (4) reference electrode (RE), (5) counter electrode (CE, here a gold coil), (6) Pyrex beaker with electrolyte (0.1 M KOH at 12 mbar), (7) beaker holder with XYZ movement, (8) end-piece of the wobble stick used for capping the Ti cone (2) during venting of the analysis chamber, here in its parking position, (9) adjustment screws to compensate for a variable sample thickness, and (10) photodiode to measure photon flux. Taken with permission from [53]; (**c**) Ambient pressure XPS spectra acquired after dip and pull cycles with the Ir(001) sample and 0.1M KOH electrolyte at different potentials relative to the RHE scale. Data recorded at the PHOENIX I beamline at 12 mbar base pressure, using a photon energy of 4000 eV. Taken with permission from [53].

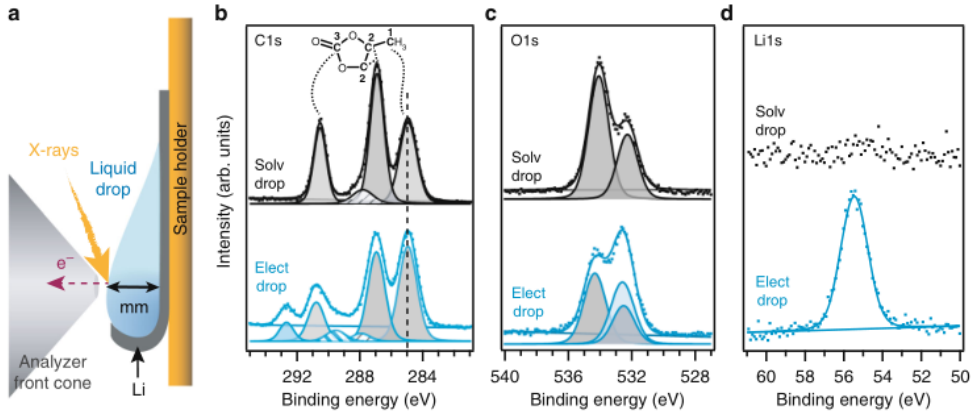

Figure 4. APPES measurements of PC solvent and 1 M LiTFSI in PC electrolyte. Schematic side view representation of the respective liquid droplets on the Li substrate (**a**). C 1s (**b**), O 1s (**c**), and Li 1s (**d**) PES spectra of Solvent drop (Solv-Drop, **top**), and Electrolyte drop (Elect-Drop, 1 M LiTFSI in PC, as prepared, **bottom**). Taken with permission from [65].

The spectra for the Elect-Drop sample are shown in the lower part of Figure 4b–d. The additional peaks in the C 1s, O 1s, and Li 1s spectra for the Elect-Drop sample are produced by the LiTFSI salt, thus enabling the effective separation of salt from solvent. While the examples discussed above demonstrate the potential of NAP-XPS for investigating electrochemical processes in liquid electrolytes, the technique was also proven equally valuable for the study of solid-state electrochemical energy conversion devices. Among these, SOCs represent one of the most investigated systems, due to their complex gas–solid interfaces and in operando conditions.

Complementarity of NAP-XPS with Other Operando Characterization Techniques for SOCs

Although NAP-XPS is able to provide mechanistic insights into the surface chemistry of SOC electrodes under realistic gaseous environments, its findings become more relevant when combined with complementary in operando characterization techniques. The electrochemical performance and degradation of SOC electrodes arise, indeed, from the interplay between surface and bulk processes, defect chemistry and microstructural evolution, which cannot be comprehensively described by a single experimental method. Therefore, the analytical potential of NAP-XPS becomes more relevant when coupled to techniques, such as electrochemical impedance spectroscopy (EIS), X-ray absorption and Raman spectroscopies or hard X-ray photoelectron spectroscopy (HAXPES), that probe different length scales and physical phenomena as schematically summarized in Table 1. Within the field of SOCs, EIS is commonly used to evaluate the electrochemical performance of the electrodes as it can directly quantify polarization and ohmic losses, charge-transfer and gas diffusion processes under operating conditions. EIS data are commonly measured to evaluate the initial performance or degradation rate of SOC materials from cell to stack level. Additionally, EIS data can be analyzed by the distribution of relaxation times technique (DRT) to address the resistive peaks to their underlying physical phenomena [68–72]. Nonetheless, EIS data do not provide direct structural information on electrode materials, thus requiring integration with surface and bulk-sensitive techniques. In this context, X-ray absorption spectroscopy (XAS) is a synchrotron-based technique which can be used to investigate the electronic and local atomic structure of SOC electrode materials under realistic operating conditions. While NAP-XPS provides surface-sensitive information, XAS is able to offer complementary bulk-sensitive insights into oxidation states, coordination environments and local structural disorder. In operando, XAS is able to monitor dynamic redox processes and phase transformations at elevated temperatures and under reactive atmospheres, allowing direct correlations between structural evolution and electrochemical performance. Furthermore, its ability to probe materials lacking long-range crystallographic order makes XAS especially suitable for studying defect-rich and nanostructured electrodes. However, XAS generally requires synchrotron radiation facilities, provides limited surface sensitivity, and its quantitative interpretation often relies on advanced spectral analysis and theoretical modeling [73–75]. In operando, Raman spectroscopy has also been employed to monitor redox processes, surface segregation and structural degradation at elevated temperatures and under reactive gas environments, thus allowing direct correlations between structural changes and electrochemical performance. Raman spectroscopy can provide complementary insights to NAP-XPS into both surface and near-surface structural evolution since it enables the identification of crystalline and amorphous phases, oxygen vacancies, and phase transitions. However, the analytical potential of this technique can be limited by fluorescence interference, the low Raman scattering cross-section of some materials and the requirement that the investigated phases exhibit Raman-active vibrational modes [75,76].

Eventually, HAXPES extends the capabilities of conventional and near-ambient pressure XPS by employing high-energy X-rays, thereby increasing the photoelectron escape

depth and enabling non-destructive characterization of inner interfaces and electrode areas. While NAP-XPS is primarily sensitive to the outermost surface, HAXPES provides complementary information on the chemical composition several tens of nanometers below the surface, thus making it particularly valuable for investigating electrode/electrolyte interfaces and interdiffusion phenomena. However, HAXPES generally requires synchrotron radiation, offers lower surface sensitivity than conventional XPS and can show reduced spectral resolution and photoionization cross-sections at high photon energies [77–79]. It is also worth adding a final consideration on spatial resolution: while Raman modern equipment and microscopy techniques like scanning transmission electron microscopy (STEM) allow obtaining spatially resolved spectra, XPS and NAP-XPS systems need specific implementation. Commercially available NAP-XPS features lateral resolution <50 µm when a µm-focus option is included [80], while synchrotron-based ESCA MICROSCOPY allows reaching a spot of 120 nm [55].

Table 1. Summary of the main advantages and limitations of NAP-XPS and complementary characterization techniques for SOC materials.

Technique	Information	Strengths	Limitations	Applications to SOCs
EIS	Electrochemical kinetics, polarization processes, ohmic resistance	Evaluation of charge-transfer and transport resistances during operation	No chemical or structural information	Reaction kinetics, degradation diagnostics, electrode and electrolyte performance
NAP-XPS	Surface composition, oxidation states, adsorbed intermediates, electronic structure	Observation of surface chemistry under reactive gases and polarization	Limited probing depth (<25 Å); operating pressure $\leq$ ~10–20 mbar [81]; model-cell geometries often required.	Surface redox, cation segregation, adsorbates, exsolution, electrode activation/degradation
HAXPES	Chemical states of inner interfaces and subsurface regions	Bridges conventional XPS and bulk-sensitive methods (enlarged probing depth up to ≈200 Å [80]), pressure ≈ 1 bar [82]	Special setup required to maintain surface sensitivity [83]. Even if not strictly necessary, synchrotron is preferable for quantitative determinations of the composition.	Buried interfaces, depth profiling, electrode/electrolyte interfaces
X-ray absorption spectroscopy	Oxidation state and local atomic coordination	Selective probing of bulk redox chemistry under operating conditions. Depth sensitivity of a few nm for the total electron yield detection method and a few hundred nm for the total fluorescence yield [84].	Limited surface sensitivity; synchrotron often required	Bulk redox, oxygen vacancy formation, local structural evolution
Raman	Vibrational fingerprints of phases and adsorbed species	Identification of molecular species and reaction intermediates. Penetration depth depends on the wavelength; e.g., for Si it increases from 6 nm at a wavelength of 244 nm to 3000 nm at a wavelength of 633 nm [85,86]. Possibility to obtain spatially resolved information.	Fluorescence, weak Raman signals, selection rules must be considered	Carbon deposition, oxygen species, phase transformations
STEM	Morphology, crystal structure, elemental distribution	Atomic-scale spatial resolution	Limited operando capability; demanding sample preparation; vacuum environment	Nanostructure evolution, exsolution, degradation, interfaces

4. NAP-XPS for Solid Oxide Cells Materials

Given the capability of NAP-XPS to elucidate reaction mechanisms, the insights which can be obtained by its application to SOC materials can have direct and significant implica-

tions for the rational design of their next-generation cells. In both air and fuel electrodes, indeed, the properties of the electrocatalytically active surface are determined by the applied operating conditions (temperature, gas phase composition, oxygen activity and applied electrochemical bias). Furthermore, within SOCs, many degradation mechanisms are surface- or interface-driven: Ni oxidation or coarsening, loss or redistribution of active metal networks, carbon deposition, formation of Sr- or Ba-rich secondary phases on air electrodes and segregation of impurities blocking electrochemically active sites [34,45,87–92].

With the purpose of elucidating the potential of NAP-XPS towards the engineering of SOC materials, the following sections cover and analyze the literature reported to date on its application to both fuel and air electrodes. Specifically, the reviewed literature studies show a progressive trend from the analysis of model surfaces towards operating electrochemical devices. Early model studies on ceria, Cu, Mn or thin film perovskites establish how NAP-XPS can follow oxidation states and adsorbates under gas and potential control. More recent works have extended the approach to more technologically relevant cermets, such as Ni-GDC and Ni-YSZ or air electrode perovskites under oxygen exchange conditions. The common strength of these studies is that they allow monitoring of the electrode surface while it is chemically and electrochemically active. This makes NAP-XPS results more meaningful since their chemical information is directly tied to electrochemical variables. In this frame, binding energy shifts can indicate changes in the local electrostatic potential, modifications in the Ce^{3+}/Ce^{4+}, Ni^{0}/Ni^{2+}, $Fe^{0}/Fe^{2+}/Fe^{3+}$ ratios or changes in the Co oxidation state due to the oxygen activity. Additionally, simultaneous impedance spectroscopy can connect surface chemistry to polarization resistance, thus shedding light on those surface species which can become either rate-limiting intermediates or active sites. A schematic illustration summarizing the role of NAP-XPS towards the understanding of the surface chemistry, degradation mechanisms and electrochemical performance of SOCs is reported in Figure 5.

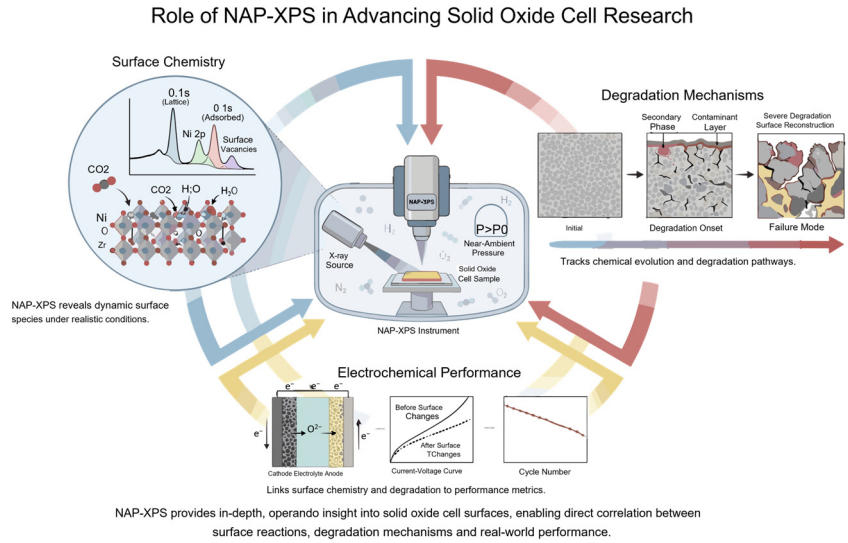

Figure 5. Illustration of the NAP-XPS role in advancing research on surface chemistry, understanding of degradation mechanisms and electrochemical performance of SOCs. Scheme created by using the image generator FigureLabs and subsequently edited by the authors.

4.1. Fuel Electrode-Related Studies

4.1.1. Ceria Model Electrodes: Redox-Active Surfaces and Extended Active Areas

Ceria thin films have been investigated as model hydrogen-electrode materials and have also been analyzed within NAP-XPS studies. DeCaluwe et al. applied APXPS on ceria/YSZ cells in H_2/H_2O mixtures between 635 and 740 °C. They showed that the

oxidation state of cerium dynamically responds to changes in temperature and oxygen partial pressure, with a transition between Ce^{4+} and Ce^{3+} states associated with oxygen vacancy formation (Figure 6a). Specifically, at zero bias, the near-surface material already contained a high fraction of Ce^{3+}, showing that the surface is more prone to reduction than bulk ceria under the same nominal conditions. The Ce^{3+} fraction increased under positive cell bias (−348 and −143 µA in Figure 6a), associated with H_2O electrolysis, while it was found to decrease under negative bias associated with H_2 oxidation (+67 and +123 µA in Figure 6a). Therefore, the Ce^{3+}/Ce^{4+} ratio was interpreted not only as a marker of the redox dynamic equilibrium, but also as a direct indicator of the local oxygen vacancy concentration generated under electrochemical operation [93]. In general, for comparable magnitudes of cell bias, the positive currents associated with H_2 oxidation were found to be smaller than the negative currents observed during H_2O electrolysis. Simultaneous electrochemical and XPS measurements indicated that a highly reduced ceria surface is more active for electrolysis and suggested that surface reactions on ceria can partially limit the overall electrochemical currents.

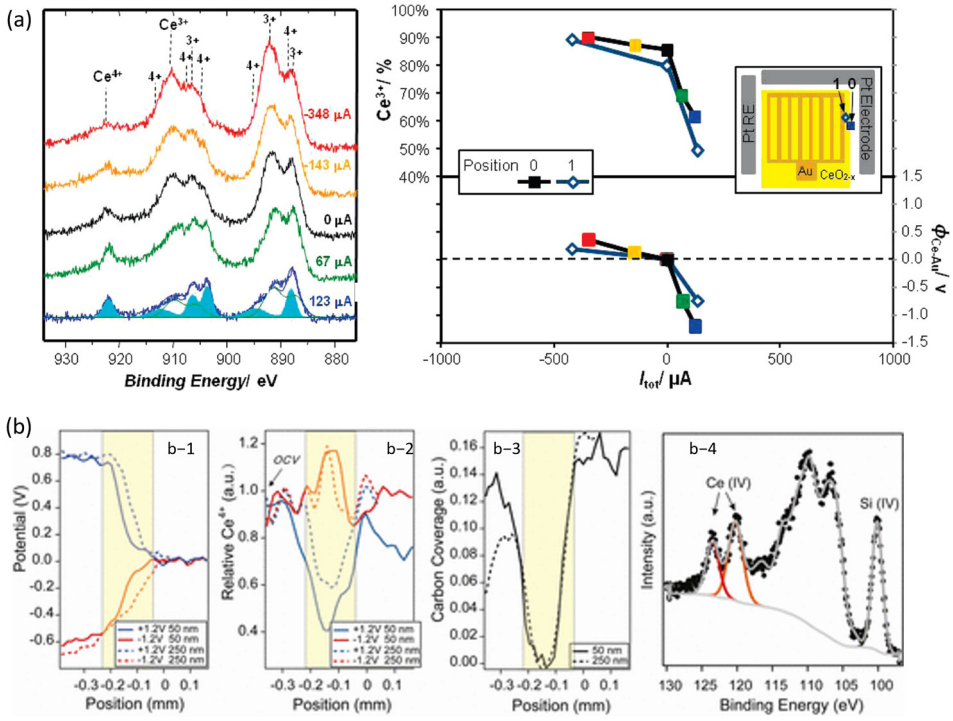

Figure 6. (**a**) Ce 3d XPS spectra from CeO_{2-x} closest to Pt cathode with varying current density during cell operation (**left** image) and measured percentage of Ce^{3+} and ϕ_{Ce-Au} (i.e., ϕ_{Ceria}) from the XPS spectra fitting as a function of total current through the ceria electrode (**right**) for cell operation at 635 °C, P_{H2} = 0.25 Torr, and P_{H2O} = 0.25 Torr. Adapted and reproduced with permission from [93]; (**b**) Signatures of the electrochemically active regions (yellow boxes) on the investigated 50 nm and 250 nm thick ceria electrodes; (**b-1**): surface potentials calculated from the kinetic energy shifts in Si 2p spectra, showing significant potential drops close to the Au current collectors located at 0 mm; (**b-2**): relative concentrations of Ce^{4+} measured in operando at +1.2 V and −1.2 V. The concentration values are normalized to the equilibrium OCV value, which is defined as 1.0; (**b-3**): relative carbon concentration on the cell surface, showing absence of carbon in the active regions; (**b-4**): A cross-sectional slice of Ce 4d spectrum (black dots) with two components associated only with Ce^{4+} and a Si^{4+} peak (Si 2p) at ∼100 eV. Adapted and reproduced with permission from [94].

Spatially resolved APXPS studies on ceria/YSZ/Pt model cells complemented these results by mapping local electrochemical activity. Shifts in the Ce^{3+}/Ce^{4+} ratio, surface potential losses and the removal or transformation of surface impurities revealed that

the electrochemically active region on ceria can extend beyond TPB sites. Depending on cell geometry and the design of the experiment, activity was reported over length scales ranging from hundreds of nanometers to roughly 100–200 micrometers from the active interface region [94,95], as shown in Figure 6b.

4.1.2. Ni-GDC Fuel Electrodes: Coupled Ni and Ceria Redox During Activation

The NiO-GDC studies by Nurk et al. modify the ceria model layers into a cermet fuel electrode. In the dual chamber HT-NAP-XPS/impedance setup, reduction in NiO-GDC to Ni-GDC in a NiO-GDC/GDC/LSC complete cell was monitored while controlling the working electrode potential and oxygen partial pressure. The key observation is a simultaneous evolution of the Ni 3p, Ce 4d and O 1s spectra with impedance: Ni^{2+} is reduced to metallic Ni, while Ce^{4+} is partially reduced to Ce^{3+}. This coupled redox chemistry accompanies the formation of an electronically conductive Ni network and the associated decrease in electrode resistance [96,97]. Furthermore, it was also reported that the applied electrochemical polarization can shift the NiO/Ni equilibrium similarly to what would be expected from the gas phase diagram. In this frame, polarization of the cermet fuel electrode at open circuit voltage (OCV) was reported to promote NiO reduction at oxygen partial pressures higher than those predicted thermodynamically for an unpolarized surface. Therefore, it can be concluded that the Ni-GDC activation could be considered as an electrochemical redox process, not only as chemical reduction by hydrogen. Additionally, compared to the reference Ni-YSZ cermets, Ni-GDC composites have two coupled redox reservoirs: NiO/Ni^{2+} and Ce^{3+}/Ce^{4+}. On one side, this aspect can be beneficial during operation since ceria can expand the reactive electrode region and buffer oxygen activity, but, on the other side, it also means that the operating state of the electrode can depend on ceria non-stoichiometry.

4.1.3. Ni-YSZ Fuel Electrodes: Ni Oxidation, Surface Redistribution and Water Electroreduction

The Ni-YSZ cermet is the reference state-of-the-art fuel electrode, and the NAP-XPS literature shows that its surface is chemically dynamic even under relatively simple gas treatments. Specifically, Paloukis et al. compared Ni/YSZ with a La-Sr-Cr-Fe-based perovskite in oxidizing, reducing and humid environments. Using synchrotron-based NAP-XPS and X-ray absorption spectroscopy, the authors investigated how oxidizing, reducing and humid atmospheres impact the chemical state, surface composition and electronic structure of these materials. The results showed that both electrode types undergo surface restructuring when exposed to reactive gas environments. For Ni/YSZ, gas switching affected both the Ni oxidation state and the near-surface composition. Additionally, the electrode surface resulted enriched in the YSZ phase, which was attributed to Ni shrinkage upon reduction and morphological changes such as porosity formation during redox cycling [98], with shrinking of Ni being expected due to the higher surface energy of metallic Ni.

A more recent study on in operando Ni/YSZ electrodes under H_2O electroreduction focused on the analysis of the electrolysis-relevant surface. Modified miniature cells allowed direct spectroscopic probing of the functional electrode region close to the YSZ interface. The authors established a correlation between the nickel surface oxidation state and H_2O electroreduction performance. Notably, the oxidized Ni phase formed during H_2O electrolysis was assigned to NiO rather than $Ni(OH)_x$, based on the Ni L-edge, Ni 2p and O 1s evidence. Depth-sensitive soft and hard XPS further indicated that Ni and NiO are uniformly mixed at the surface under electrolysis conditions, rather than forming a Ni-core/NiO-shell structure typical of gas-phase oxidation, as shown in Figure 7 [99]. This finding also illustrates that nickel oxidation under steam shapes a redistributed mixed Ni/NiO surface in which metallic Ni remains partly accessible. This aspect becomes

particularly relevant for phase percolation, since the electrochemical performance depends on how much metallic Ni, NiO and YSZ remain connected to gas, electron and oxide-ion pathways near the active interface.

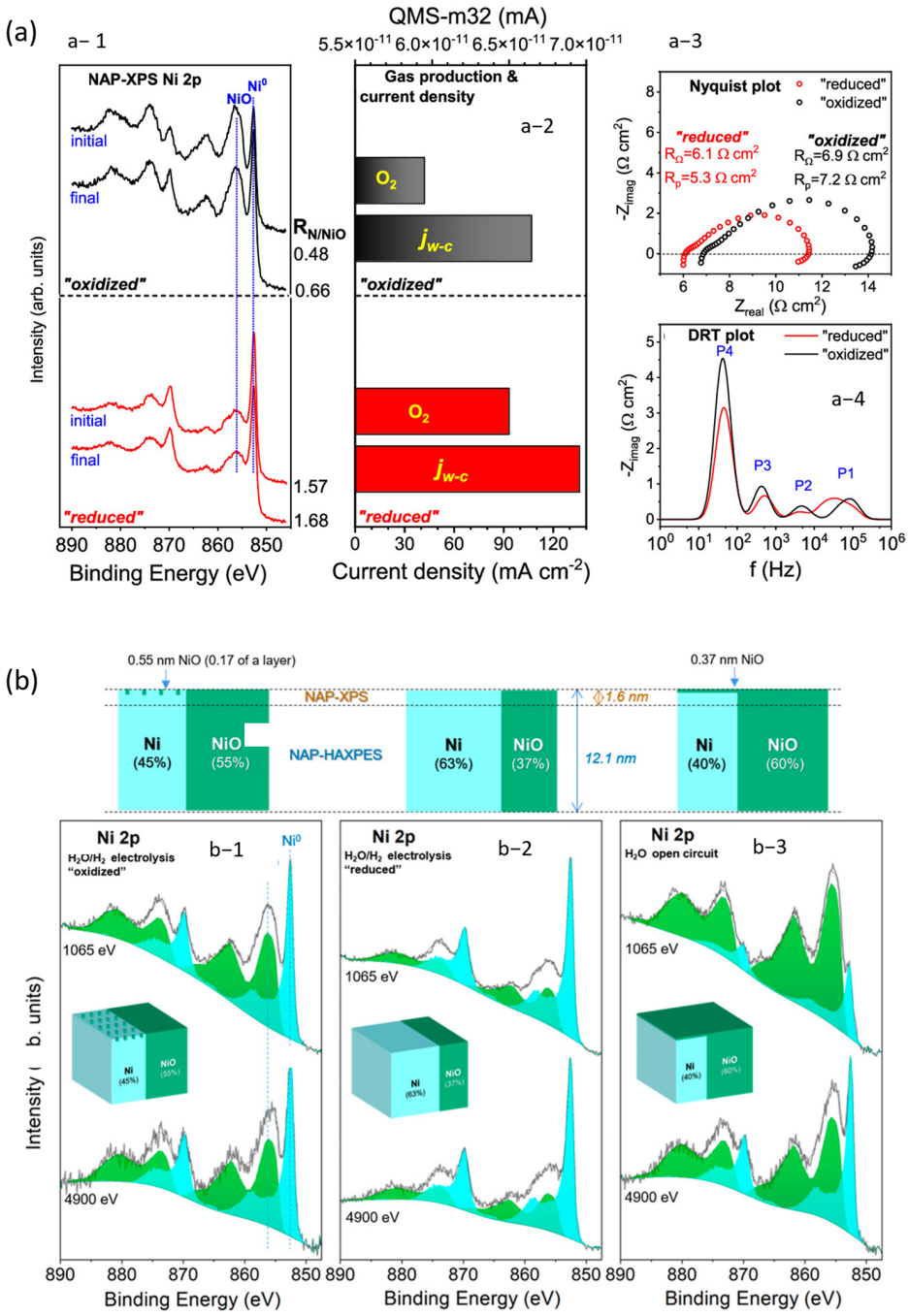

Figure 7. (**a**) (**a-1**) In operando Ni 2p ($h\nu$ = 1065 eV) NAP-XPS spectra measured under electrolysis conditions (E_{W-C} = 2.5 V, pH_2O/pH_2 = 9:1 at 750 °C), (**a-2**) mean current density of the cell and the production of gas-phase O_2 measured on line during the photoemission experiments of (**a-1**). Impedance spectra presented as (**a-3**) Nyquist and (**a-4**) DRT plots for the two cells. Adapted and reproduced with permission from [99]. (**b**) Ni 2p core-level spectra measured using 1065 eV (NAP-XPS) and 4900 eV (NAP-HAXPES) photon energies over the Ni/YSZ electrode during E_{W-C} = 2.5 V, 1 mbar H_2O/H_2 = 9:1 at 750 °C (after mild reduction pretreatment, (**b-1**), E_{W-C} = 2.5 V, 1 mbar H_2O/H_2 = 9:1 at 750 °C (after harsh reduction pretreatment, (**b-2**), and open circuit, 1 mbar H_2O at 750 °C (after previous reduction in H_2), (**b-3**). Adapted and reproduced with permission from [99].

4.1.4. CO_2 and CO_2/H_2O Electrolysis on Model Metal Electrodes: Carbon and CO Chemistry

The studies of Bozzini et al. on Cu and Mn model electrochemical systems show how NAP-XPS and Near Edge X-ray Absorption Fine Structure (NEXAFS) can follow carbonaceous deposits, adsorbed CO, metal oxidation states and electrolyte interface degradation under controlled gas exposure and polarization.

In the study on Cu electrodes, the authors investigated the surface chemistry of copper during the electrochemical reduction in CO_2 in a model solid oxide electrolysis cell by means of NAP-XPS and NEXAFS measurements under in operando conditions. The experiments were performed at 600 °C while applying electrochemical polarization in CO_2 and CO_2/H_2O atmospheres. They observed that the surface chemistry of Cu evolves dynamically during operation. Specifically, in dry CO_2, pre-existing carbon deposits were found to be removed at lower cathodic potentials (≈2 V) due to the role played by the oxygen generated during CO_2 reduction, which oxidized and eliminated the carbon. Conversely, at higher cathodic polarizations (≈ 4 V), carbon was detected on the cathode surface due to the reduction in CO. On the other hand, in dry CO_2, no surface C-O species were detected. However, in CO_2/H_2O mixtures, a carbon deposit was found to be maintained within the investigated potential range and adsorbed CO was also detected. Therefore, the presence of water changed the reaction network by enabling H_2- or H_2O-assisted CO_2 conversion and stabilizing CO/carbon-related surface species [100].

Within the Mn thin film study, the authors investigated the surface chemistry of miniaturized manganese electrodes deposited over a YSZ supporting electrolyte in a Cu/YSZ/Mn cell under different gas environments (CO_2, CO_2/H_2O and H_2O) at 600 °C. This work studies how the oxidation state and surface composition of Mn evolve under electrochemical polarization (SOEC mode). The results showed that the manganese oxidation state also strongly depends on the applied potential and reaction environment, with more oxidized Mn species forming under anodic conditions. MnO was found to be the stable chemical form at OCV, while Mn_3O_4 was detected under anodic polarization in all the investigated gas atmospheres (i.e., under CO_2, CO_2/H_2O and H_2O). The experiments also revealed the formation and removal of carbonaceous surface species depending on the gas composition, similarly to what was observed for Cu-based films. Under strong anodic polarization (i.e., applied voltage of 4 V), the reduction in zirconia and the formation of zirconium carbide were also detected, indicating degradation processes at the electrode-electrolyte interface [101]. Both Cu- and Mn-based model film studies show that CO_2- and co-electrolysis cannot be discussed only in terms of the oxidation state of the main electrode metal, since carbon, CO, surface species and local oxygen activity form a coupled reaction network. Additionally, the reaction mechanism is strongly influenced by the applied bias, thus suggesting the establishment of different reaction pathways according to the applied operating conditions.

4.1.5. Exsolving Perovskite Fuel Electrodes: Activation and Surface Chemistry

Recent investigations on fuel electrodes have also addressed the partial replacement of the Ni cermet with redox-stable mixed-conducting perovskites that exsolve active metal nanoparticles under reducing conditions. In this frame, Nurk et al. investigated $La_{0.31}Sr_{0.58}Ti_{0.97}Ni_{0.03}O_{3-\delta}$ (LSTN3) thin film electrodes in two studies. Specifically, in their first work, they carried out NAP-XPS measurements at high temperature and under reactive gas atmospheres relevant to SOEC/SOFC operation to investigate the surface chemistry of thin LSTN3-based electrodes (prepared by pulsed laser deposition). The results mainly revealed that Ni exsolves from the perovskite lattice and forms metallic nanoparticles on the electrode surface under reducing conditions (−1 V vs. OCV at 850 °C in 3% H_2O + 97% H_2 environment at 3 mbar total pressure) [102]. In the second study, thin film electrodes of

the same material were analyzed at 650 °C with a 0.5 mbar total pressure under three gas compositions: 1.6% H_2O + 98.4% H_2, 12% H_2O + 88% H_2, and 42% H_2O + 58% H_2 [103]. The electrode polarization was varied from 0 to +0.4 V using photon energies of 600 and 1000 eV. The results suggest that the electrochemical activity of the LSTN3 surface increases with increasing water concentration in the gas phase. The NAP-XPS analysis also shows that Ti surface species undergo changes in the Ti^{3+}/Ti^{4+} ratio depending on the oxygen activity, indicating that the surface redox chemistry responds to the gas environment and polarization conditions. Specifically, a rutile-like TiO_2-terminated surface structure was identified under reducing conditions, and narrower Ti $2p^{3/2}$ and $2p^{1/2}$ peaks were detected with increasing H_2O concentration or anodic polarization, with more pronounced changes at the surface than in the bulk. Furthermore, a change in electrochemical kinetics observed at approximately 0.3 V was attributed to the oxidation of exsolved Ni nanoparticles on the surface (as also observed in their previous study). The La and Sr XPS spectra were found to be largely independent of electrode polarization but strongly dependent on the water content in the gas phase. In particular, the formation of surface $La(OH)_3$ species increased with higher water concentration, correlating also with the measured electrochemical activity. Globally, these studies underlined that exsolving LSTN3 electrodes have at least two relevant states: the activation one, in which nanoparticles or surface metallic species are generated and the operating surface state, in which water content, oxygen activity and polarization modify Ti, La/Sr hydroxylation and Ni oxidation.

4.2. Air Electrode-Related Studies

4.2.1. Sr and Ba Surface Chemistry: Enrichment, Active Sites and Blocking Phases

The existing literature on SOCs air electrodes reports that alkaline earth enrichment can be associated with high oxygen exchange activity but, at the same time, with secondary phases blocking active sites and driving degradation [34,89,90,104]. By means of NAP-XPS, the studies reported in the following paragraph analyze the effect of different dopants on the electrode surface chemistry under multiple operating conditions.

Crumlin et al. compared epitaxial LSC (001) thin films with polycrystalline LSC pellets in order to understand the origin of their different catalytic activities [105]. APXPS measurements were performed from room to 520 °C and near-ambient oxygen pressures, allowing the authors to map the evolution of surface composition under quasi-realistic operating conditions. The results showed that the LSC thin film undergoes significant surface reconstruction when increasing temperature, including reduction in surface secondary phases and enrichment of Sr at the surface. In contrast, the polycrystalline pellet exhibited little deviation in surface composition under the same conditions. Specifically, when heated to 520 °C at a moderate oxygen partial pressure (10^{-3} atm), the LSC film surface exhibited (i) lower coverage of secondary surface phases compared to the pellet surface and (ii) Sr enrichment within the perovskite lattice in the near-surface region (while the pellet surface showed no detectable lattice Sr enrichment). These differences were used to explain the higher oxygen electrocatalytic activity observed for LSC (001) films compared to LSC powders, being partly addressed to the reduced coverage of secondary phases and the formation of Sr-enriched perovskite surface sites at elevated temperatures. Nonetheless, the same paper notes that secondary surface phases can enhance oxygen exchange at low coverage while reducing activity at high coverage. More generally, other LSC/LSCF studies associate Sr-rich oxide, hydroxide or carbonate-like phases with blocking of transition metal sites and loss of oxygen exchange performance [34,89–92]. From a broader perspective, this study highlights that electrode performance can be distinctly affected by three chemically different situations: Sr incorporated in a perovskite near-surface lattice, Sr-rich secondary

phases at low coverage, and thick or poorly conducting Sr-rich deposits that block Co/Fe active sites.

The Ba-containing layered perovskite $NdBa_{1-x}Co_2O_{5+\delta}$ represents another electrode material where doping elements affect structural stability during typical SOC operation. Bozzini et al. investigated the surface chemistry of the layered perovskite $NdBa_{1-x}Co_2O_{5+\delta}$ as a candidate cathode for SOFCs [106]. Measurements were performed at 800 K on symmetric cells with a GDC electrolyte under oxygen atmospheres and applied electrochemical bias. The results revealed that the oxygen reduction reaction on this material proceeds despite the presence of chemisorbed molecular oxygen species on the cathode surface. This study identified partially reduced barium species as the active sites responsible for oxygen reduction on the $NdBa_{1-x}Co_2O_{5+\delta}$ surface. The molecular oxygen species was found not to be significantly influenced by the degree of Ba deficiency, supporting the conclusion that O_2 adsorption on Ba^{2+} surface sites represented the initial step of the ORR mechanism on $NdBa_{1-x}Co_2O_{5+\delta}$. Nevertheless, Ba deficiency was also observed to affect surface composition. In particular, the surface concentration of BaO, namely the detected dominant Ba-containing surface species, gradually decreased as Ba deficiency increased. Conversely, cobalt oxides, due to the stabilization of higher Co oxidation states, and BaO_2, associated with the intermediate step of partial oxygen reduction, became more abundant. Furthermore, the changes observed in the oxygen chemical state were consistent with charge-compensation mechanisms governed by Ba deficiency. Increasing the oxygen partial pressure led to a decrease in the concentration of Ba oxides, in agreement with the Ba-O_2 adsorption model proposed by the authors. Finally, operando measurements showed that prolonged operation leads to surface aging characterized by the formation of defective cobalt oxide phases and a progressive depletion of the active Ba surface species. Therefore, in this material, Ba was found to behave not simply as a segregating impurity since it is implicated directly in O_2 adsorption/reduction and its depletion and replacement by defective Co oxides contribute to aging.

4.2.2. Vacancy Channels, Crystallographic Orientation and Transition-Metal Redox

The NAP-XPS technique was also used to demonstrate that oxygen electrode activity depends on the structural vacancy pathway. In particular, Hong et al. studied the high-temperature surface chemistry of epitaxial $Sr_2Co_2O_5$ (SCO) thin films [107]. The experiments were carried out on epitaxial thin films of 25 nm fabricated by pulsed layer deposition and tested in an oxygen atmosphere between 300 and 600 °C. NAP-XPS measurements indicated that increasing temperature leads to oxygen loss from the surface, as evidenced by changes in the Co 2p spectra and O 1s features. Detailed analysis of the oxygen spectra showed different surface species whose relative contributions varied with temperature. Additionally, the study demonstrated that surface chemistry strongly depends on the crystallographic orientation of the thin film. In particular, films with (114) orientation exhibited an additional oxygen species associated with a perovskite-like surface environment, which was not observed for the (001) orientation. This difference was mainly attributed to the orientation of oxygen vacancy channels with respect to the surface, which can affect oxygen transport and surface exchange processes. Therefore, the active oxygen surface is not determined only by nominal composition, such as Sr/Co ratio or Co valence, but also depends on whether the crystal orientation connects the vacancy channels in a way that facilitates oxygen exchange.

A broader perovskite comparison by Nenning et al. examined LSC, LSF and STF thin film electrodes under controlled polarization. In particular, the authors combined NAP-XPS with simultaneous impedance spectroscopy and stationary electrochemical analyses to allow for direct correlation between surface chemical states and electrochemical activity (see

Figure 8). The experiments underscored the presence of additional surface species involving strontium and oxygen on all investigated materials under oxidizing conditions, indicating the presence of a Sr-rich surface termination commonly found in perovskite electrodes. Specifically, in oxidizing atmospheres, all three materials showed high-binding-energy Sr and O surface components consistent with SrO and/or $Sr(OH)_2$-like surface species. LSC displayed metal-like valence band behavior, whereas LSF and STF showed localized electronic defects and thermally activated electronic conductivity. In reducing H_2/H_2O atmospheres, LSF and STF displayed Fe redox: Fe^{3+} under oxidizing conditions, mixed Fe^{2+}/Fe^{3+} in reducing conditions and reversible Fe^0 formation under cathodic polarization. The latter was linked to enhanced water splitting activity, in particular for LSF [108]. The combined analysis of different materials allowed several effects that are often merged when analyzing perovskite electrodes, namely alkaline-earth surface termination, transition metal redox, electronic structure shifts caused by oxygen chemical potential, and true electrochemical polarization effects.

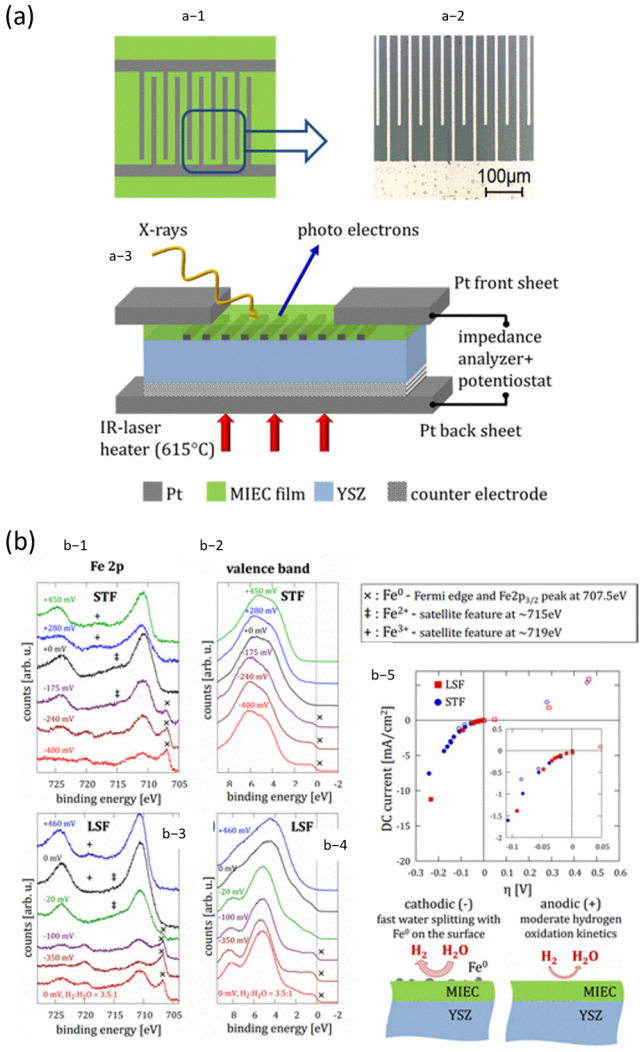

Figure 8. (**a**) Sketch of the entire working electrode surface (**a-1**) and photograph of a part of it (**a-2**); (**a-3**): Sketched cross section of the sample and mount in the ambient XPS chamber; (**b**) Fe 2p and valence band XPS spectra of STF (**b-1**,**b-2**) and LSF (**b-3**,**b-4**) polarized by different overpotentials in H_2/H_2O atmosphere. The applied overpotentials are indicated for each spectrum. (**b-5**) DC-characteristics of LSF (red squares) and STF (blue circles). When Fe^0 is present during cathodic polarization (filled symbols), the current increases strongly nonlinearly, even at very small bias (inset). Adapted and reproduced with permission from [108].

4.2.3. Surface Modification and Hybrid Cathodes

Surface engineering of SOCs electrodes is usually performed to enhance their electrochemical performance by the addition of active nanoparticles and/or suppress degradation mechanisms. In this frame, LSCF modified with a $PrNi_{0.5}Mn_{0.5}O_3$ thin film featuring exsolved PrOx nanoparticles was reported to show lower polarization resistance than standalone LSCF [109]. Specifically, the polarization resistance of the coated LSCF electrode was found to be 1/6 of the uncoated one. The improved electrochemical performance was ascribed to the beneficial effects played by (i) the high concentration of oxygen vacancies on the surface of PrOx nanoparticles, which accelerate the charge transfer process and (ii) the quicker ion transport and surface stability of LSCF promoted by the $PrNi_{0.5}Mn_{0.5}O_3$ thin film. The latter was also found to suppress Sr segregation from LSCF. Furthermore, this study demonstrates that the electrode surface undergoes continuous restructuring, with significant changes in oxidation states and adsorbed species depending on the gas phase composition. These results are consistent with previous NAP-XPS findings: well-designed air electrodes require reactive oxygen vacancy chemistry, but also suppression or control of blocking alkaline-earth surface phases. Furthermore, they underlined the importance of in operando surface characterization for identifying active species and elucidating reaction pathways in SOC electrodes. Combined NAP-XPS, catalytic testing and impedance spectroscopy analyses allowed measuring surface chemical states, catalytic rates and electrochemical response under comparable conditions. This approach reduces the risk of assigning XPS-observed species as active or detrimental without a direct activity correlation [110,111]. In this frame, Rameshan et al. investigated the role of defect chemistry and surface processes in determining the performance of an electrochemical model cell (including $Nd_{0.6}Ca_{0.4}Fe_{0.9}Co_{0.1}O_3$ as working electrode) by simultaneous NAP-XPS, catalytic and electrochemical characterizations [111]. By combining experimental observations with theoretical analyses, the study provided insights into how point defects (e.g., oxygen vacancies and cation non-stoichiometry) affect surface exchange kinetics and catalytic activity (see Figure 9a,b). The results showed that surface defect concentrations and their interaction with the gas phase impact the electrochemical performance. The ion mobility in the electrolyte and the oxygen exchange activity were found to increase with the operating temperature and the applied cathodic bias. In addition, this work highlighted that surface chemistry can deviate from bulk defect equilibria, thus reinforcing the importance of surface-sensitive techniques to gain insight into electrode reaction pathways. Studying the exsolution behavior of $Nd_{0.6}Ca_{0.4}Fe_{0.9}Co_{0.1}O_3$, they also found that metallic Co is exsolved when applying a lower operating temperature (500–600 °C) at OCV in a H_2-H_2O atmosphere. Conversely, when increasing the operating temperature and applying cathodic potential (−250 mV), Fe also exsolved from the lattice of the perovskite.

In another study, Opitz et al. investigated the surface chemistry and oxygen exchange kinetics of strontium-doped $LaCoO_3$ (LSC). Their results showed that oxygen exchange is strongly governed by surface defect concentrations, cation composition and the presence of adsorbed oxygen species [110]. In particular, surface segregation of cations and formation of surface defects were identified as key factors controlling reaction kinetics (Figure 9c,d). In situ NAP-XPS measurements were conducted between 400 and 790 °C, while simultaneous EIS were performed to characterize the catalytic activity of the LSC electrode surface for O_2 reduction. These experimental analyses outlined that the loss in electrocatalytic activity of LSC could be ascribed to the appearance of a secondary La-containing Sr-oxide species at its surface (already between 450 and 500 °C). This was also found to preferentially cover electrochemically active Co sites at the surface, thereby significantly decreasing the oxygen exchange of LSC.

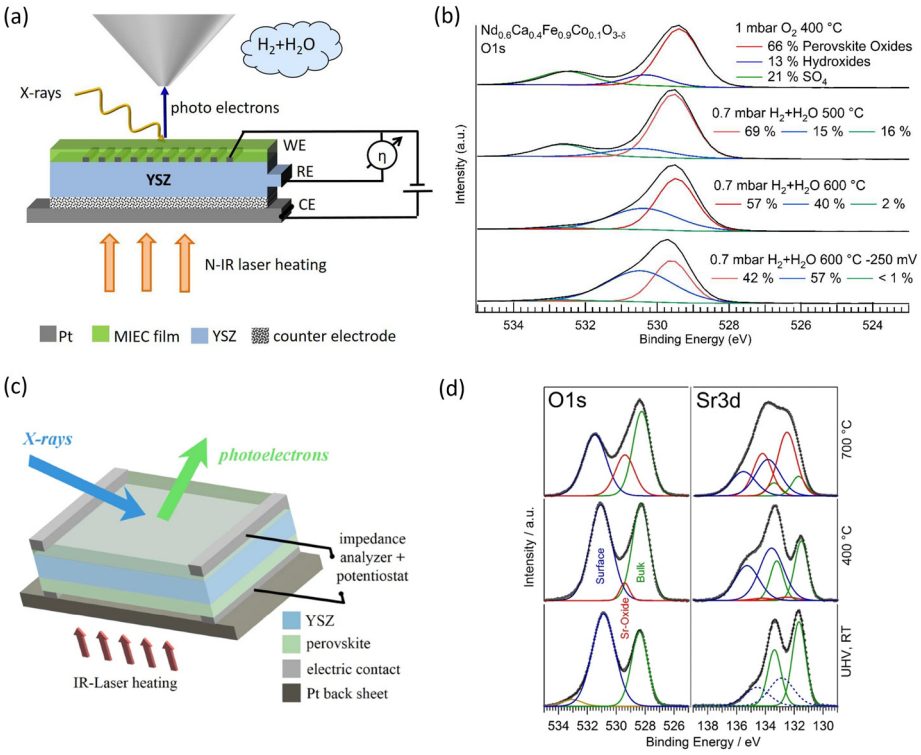

Figure 9. (**a**) Schematic presentation of the sample during measurements; (**b**) Fe 2p $^{3/2}$ signals for each experiment step. The contributions are assigned to Fe^0 (red) and a combination of two components for the asymmetric oxide peak (blue and green). A stepwise increase in the contribution of metallic Fe emerges with increasing strength of reduction. (**c**) Sketch of the sample design for the in situ experiments to allow simultaneous NAP-XPS and electrochemical impedance measurements; (**d**) XPS spectra including peak fitting for the LSC electrode surface. The bottom spectra show the surface state of the virgin, water-treated sample directly after introduction into the UHV system at room temperature. For both O 1s and Sr 3d, the green component corresponds to the perovskite bulk signal of LSC. The blue component represents the surface signal of the perovskite. The additional red peaks of the degraded state result from the formation of a third Sr-oxide compound on the surface; Adapted and reproduced with permission from [110,111].

5. Deduced Insights and Identified Limitations from NAP-XPS Studies on Solid Oxide Cell Materials

The comparative analysis of the studies considered in this review shows that NAP-XPS can provide advanced surface characterization and reveal a set of recurring mechanisms that extend through different classes of SOC electrodes. The first repeating process is the dynamic redox response of reducible oxides. In ceria-based electrodes, the Ce^{4+}/Ce^{3+} ratio changes with temperature, gas composition, oxygen chemical potential, and electrochemical polarization. This response is directly connected to the formation of oxygen vacancies and the mixed ionic-electronic conductivity of the material, thus also explaining why the electrochemically active region in ceria-based fuel electrodes can be extended beyond TPB lines. Similar redox sensitivity is observed in Ni-GDC electrodes, where the reduction in NiO to metallic Ni is accompanied by partial reduction in ceria and a corresponding change in electrochemical impedance. A second mechanism concerns the chemical instability and redistribution of nickel-containing fuel electrodes. In Ni-GDC, the reduction in NiO forms the metallic Ni network required for electronic conduction and electrode activation. In Ni-YSZ, exposure to H_2/H_2O atmospheres and water electroreduction conditions can induce dynamic changes in Ni oxidation state and surface composition. Furthermore, more recent measurements indicated that NiO formation during H_2O electrolysis does not follow the representation of a NiO shell surrounding a metallic Ni core. Ni and NiO

can, indeed, be distributed more uniformly in the near-surface region. This suggests that Ni oxidation, Ni redistribution and electrochemical performance are closely coupled and interdependent phenomena.

A third mechanism is the formation, transformation or removal of adsorbed carbon- and oxygen-containing surface species. Model studies on Cu and Mn electrodes under CO_2, CO_2/H_2O and H_2O atmospheres demonstrated that carbonaceous deposits, adsorbed CO, oxygen species and metal oxidation states evolve with both gas composition and polarization. These results become relevant for CO_2 electrolysis and co-electrolysis, where electrode poisoning and self-cleaning processes may coexist depending on the local chemical potential of oxygen and the availability of gas species. Although such systems are simplified with respect to practical SOC electrodes, they still provide mechanistic insight into how NAP-XPS identifies transient surface intermediates that would not be observable after operation.

A fourth process is cation redistribution in perovskite and perovskite-related electrodes. In air electrodes such as LSC, LSCF-related materials and layered cobaltites, the surface concentration and chemical state of alkaline-earth cations such as Sr or Ba can change substantially under high-temperature oxidizing conditions. However, these phenomena must be interpreted carefully. Sr enrichment within a perovskite-like near-surface environment can be associated with enhanced oxygen electrocatalysis in some model systems, while the formation of secondary Sr-rich phases can block catalytically active transition metal sites and contribute to degradation. In Ba-containing layered perovskites, NAP-XPS has further shown that partially reduced Ba species and chemisorbed molecular oxygen can participate in the oxygen reduction mechanism, while aging may lead to depletion of active Ba sites and enrichment in less active cobalt oxide phases. Finally, studies on exsolution-based perovskites introduce an additional type of dynamic surface process. In Ni-doped titanate electrodes, reducing conditions and electrochemical activation can promote the emergence of catalytically active Ni species at the electrode surface, while the oxide host itself undergoes changes in surface termination and transition metal redox state. These observations suggest that future SOC electrodes may be designed as adaptive surfaces whose active state is generated, regenerated or stabilized under ad hoc operating conditions designed to ensure durability. Eventually, across all the examined examples, the central contribution of NAP-XPS appears to be its ability to connect surface composition, oxidation state and electrochemical function within a single experimental framework. The schematic summary of the materials, conditions and mechanisms identified by NAP-XPS analyses is reported in Table 2.

On the other side, despite demonstrating the potential of NAP-XPS for investigating SOC materials under reactive atmospheres, the studies discussed in this review also highlight that their results must be interpreted within the limits of the employed experimental configurations. In multiple cases, the systems investigated are model electrodes, thin films, patterned microcells, single-chamber or dual-chamber devices specifically designed to satisfy the geometrical and analytical requirements of photoelectron spectroscopy. Despite these configurations allowing the surface of the working electrode to be directly exposed to the X-ray beam, they also simplify the complexity of real porous electrodes. NAP-XPS probes the outer nano-layer of the electrode surface, or slightly deeper regions when hard X-ray photoelectron spectroscopy is used. This allows for investigating adsorbates and surface processes but also entails that the measured composition can differ substantially from that of the bulk electrode. Therefore, changes in binding energy, cation concentration or oxidation state should not be directly interpreted as representative of the entire electrode volume unless supported by complementary bulk-sensitive techniques.

Table 2. Summary of the main insights obtained by the reviewed studies on NAP-XPS for SOC materials.

Material/System	Operating Conditions and Characterizations	Main Results	Refs
Ceria thin-film electrodes	H_2/H_2O, 635–740 °C, APXPS under bias	Ce^{3+}/Ce^{4+} tracks oxygen-vacancy density and bias; active region can extend beyond TPB.	[93–95]
NiO-GDC/Ni-GDC	650 °C, controlled pO_2, H_2, HT-NAP-XPS + EIS	NiO reduction to Ni couples with Ce^{4+} reduction to Ce^{3+} and impedance decrease; applied polarization shifts reduction behavior.	[96,97]
Ni-YSZ	Oxidizing/reducing/humid gases; H_2O electroreduction; 250–600 °C; NAP-XPS/NAP-HAXPES, NEXAFS and EIS	Ni oxidation state and surface composition respond dynamically to the operando atmosphere; in H_2O electrolysis, oxidized Ni becomes NiO, with mixed Ni/NiO surface distribution.	[98,99]
Cu and Mn thin films	CO_2, CO_2/H_2O, H_2O, 600 °C, NAP-XPS/NEXAFS under polarization	Cu reveals CO/carbon chemistry in co-electrolysis; Mn shows anodic MnO to Mn_3O_4 conversion and carbon removal, with prolonged-operation damage.	[100,101]
LSTN3	650–850 °C in H_2/H_2O, NAPXPS, XAS and EIS	Activation generates detectable Ni phase; operating activity depends on water content, Ti^{3+}/Ti^{4+}, $La(OH)_3$ and Ni oxidation.	[102,103]
LSC (001) vs. LSC pellet	O_2, 25–520 °C, APXPS and HRXRD	High activity is linked to lower secondary-phase coverage and Sr enrichment within a perovskite-like near-surface region.	[105]
$Sr_2Co_2O_5$	O_2, 300–600 °C, orientation-dependent NAP-XPS	Surface oxygen chemistry depends on orientation of vacancy channels; (114) films show perovskite-like oxygen chemistry.	[107]
LSC, LSF, STF	O_2 and H_2/H_2O, 615 °C, NAP-HE-XPS, applied polarization and EIS	Sr/O surface species in oxidizing atmosphere; Fe redox and reversible FeO under cathodic polarization in reducing atmosphere.	[108]
$NdBa_{1-x}Co_2O_{5+\delta}$	O_2, 800 K, operando NAP-XPS	Chemisorbed molecular O_2 and partially reduced Ba participate in ORR; aging depletes active Ba and enriches defective Co oxides.	[106]

Additionally, it appears evident that experimental configurations that combine NAP-XPS with simultaneous electrochemical impedance spectroscopy enable advanced mechanistic insight under relevant operating conditions. It is recognized that this approach can provide unique insights into reaction pathways, thus representing one of the most promising directions for future in operando studies. However, such combined measurements are not yet widely implemented. In addition, despite the growing number of NAP-XPS investigations, the available studies are largely focused on a limited set of model materials and specific degradation phenomena, such as cation segregation or redox-induced changes. Further challenges emerged from the reviewed studies, including the accessibility of synchrotron-based instrumentation and the remaining pressure gap between laboratory conditions and practical device operation.

6. Conclusions and Future Perspectives

The reviewed studies have demonstrated that NAP-XPS can provide valuable insights into the dynamic behavior of SOC electrode surfaces under different operating conditions.

By means of NAP-XPS investigations, key processes such as metal redox mechanisms, oxygen vacancy formation, cation segregation and surface reconstruction have been unveiled within quasi-realistic environments. Consequently, NAP-XPS has emerged as a strategic tool to correlate traditional surface science studies, performed under vacuum conditions, with the more complex environments encountered in operating electrochemical devices.

Nonetheless, from a methodological perspective, future studies should further explore the integration of NAP-XPS with complementary techniques (e.g., EIS, XAS, Raman spectroscopy, HAXPES and/or ab initio modeling). Correlative approaches enable direct relationships to be established between electrochemical performance, bulk redox chemistry, microstructural evolution and dynamic surface transformations, thereby providing a more comprehensive understanding of reaction mechanisms and degradation processes. Future experimental platforms integrating multiple characterization techniques simultaneously are therefore expected to play an important role in SOC research. Additionally, systematic investigations employing comparable cell geometries tested under controlled gas compositions and extended aging times would contribute to establishing quantitative relationships between XPS-derived surface properties and electrochemical activity or degradation rates.

Beyond methodological developments, operando NAP-XPS studies could also target validation on realistic SOC electrode microstructures to correlate fundamental surface-science studies and practical electrode configurations. In this frame, Thurner et al. recently developed quasi 2D Ni/YSZ and NiCu/YSZ model electrodes with spectroscopically accessible TPB regions, enabling operando investigations of electrochemically active sites that are typically difficult to probe in conventional porous cermet electrodes [112]. At the same time, NAP-XPS investigations of porous Ni-based cermet electrodes have begun to reveal mechanistic insights that could not be obtained from standalone conventional electrochemical measurements. Chen et al. demonstrated that the oxidation behavior of porous Ni-YSZ and Ni-GDC electrodes in H2O- and CO_2-containing atmospheres differs substantially, showing that nickel oxidation by these gases is strongly influenced by the nature of the ceramic support rather than following a global mechanism [113]. In a subsequent study, the same group investigated ceria-promoted Ni-YSZ electrodes prepared by infiltration of nanosized CeO_x and $NiCeO_{grgamma}$ particles. The infiltrated electrodes exhibited enhanced performance during CO_2 electrolysis compared with pristine Ni-YSZ electrodes. Synchrotron-based operando NAP-XPS measurements using both soft and tender X-rays revealed the formation of an ultrathin Ni-Ce^{3+} surface layer, providing a plausible explanation for the observed catalytic promotion effect [114].

From an instrumental perspective, further technological developments are also expected to expand the applicability of operando NAP-XPS to the research on SOCs and solid-state materials for energy applications. Further reductions in the pressure gap to real operating devices, wider accessibility of laboratory-based instruments, validation on realistic porous electrodes and advanced data analysis and computational modeling are expected to progressively bridge the remaining gap between model surface-science investigations and practical electrochemical devices. To increase the maximum operating pressure, strategies exploiting hard X-rays [64,65] and reducing the distance between the sample and the nozzle [66] have already been proposed. Currently, the main limit seems to be represented by the need for special samples due to the integrated nature of the technique. More extensive use of the μm-focus option in laboratory-scale NAP-XPS and upgrades of the existing synchrotron facilities to provide smaller spots will enable the investigation of more realistic (and then inherently less homogeneous) samples.

In our opinion, further advances in SOCs understanding could be attained by integrating multiple experimental techniques into a single experimental setup: for example by including Raman spectroscopy and XPS [115] and possibly developing systems cou-

pling NAP-XPS with TEM. Ex situ TEM was, indeed, demonstrated to provide valuable experimental information when coupled to NAP-XPS [116]. Additionally, wider availability of laboratory-based NAP-XPS systems is expected to complement synchrotron-based investigations. Although laboratory instruments currently provide lower photon flux and reduced energy tunability compared with synchrotron beamlines, improvements in X-ray sources, electron optics and detector technology could progressively extend their analytical capabilities. This evolution could facilitate routine investigations, long-term aging experiments and the screening of novel electrode materials, while synchrotron facilities will remain essential for high energy resolution measurements.

Finally, operando NAP-XPS experiments are generating increasingly large and multidimensional datasets, in which spectra are acquired as a function of temperature, gas composition, electrochemical polarization and time. Advanced data analysis strategies, including automated fitting procedures, would accelerate data processing and facilitate the identification of chemical changes that are difficult to resolve using conventional approaches. Overall, future progress in operando NAP-XPS for SOC research will rely on the simultaneous evolution of instrumentation, experimental methodologies and correlative characterization strategies. Further reductions in the pressure gap to real operating devices, wider accessibility of laboratory-based instruments, validation on realistic porous electrodes and advanced data analysis and computational modeling are expected to progressively bridge the remaining gap between model surface-science investigations and practical electrochemical devices.

Author Contributions: D.C.: writing—original draft preparation; investigation; L.V.: writing—review and editing; methodology; supervision. All authors have read and agreed to the published version of the manuscript.

Funding: This research received no external funding.

Data Availability Statement: No new data were created or analyzed in this study. Data sharing is not applicable to this article.

Conflicts of Interest: The authors declare no conflicts of interest.

References

1. Venkataraman, V.; Pérez-Fortes, M.; Wang, L.; Hajimolana, Y.S.; Boigues-Muñoz, C.; Agostini, A.; McPhail, S.J.; Maréchal, F.; Van Herle, J.; Aravind, P.V. Reversible solid oxide systems for energy and chemical applications—Review & perspectives. *J. Energy Storage* **2019**, *24*, 100782. [CrossRef]
2. Wan, Z.; Tao, Y.; Shao, J.; Zhang, Y.; You, H. Ammonia as an effective hydrogen carrier and a clean fuel for solid oxide fuel cells. *Energy Convers. Manag.* **2021**, *228*, 113729. [CrossRef]
3. Bierschenk, D.M.; Wilson, J.R.; Barnett, S.A. High efficiency electrical energy storage using a methane–oxygen solid oxide cell. *Energy Environ. Sci.* **2011**, *4*, 944–951. [CrossRef]
4. Wendel, C.H.; Kazempoor, P.; Braun, R.J. A thermodynamic approach for selecting operating conditions in the design of reversible solid oxide cell energy systems. *J. Power Sources* **2016**, *301*, 93–104. [CrossRef]
5. Lamagna, M.; Groppi, D.; Nastasi, B. Reversible solid oxide cells applications to the building sector. *Int. J. Hydrogen Energy* **2023**, *48*, 27033–27058. [CrossRef]
6. Jiménez-Martín, G.; Bąkała, M.; Judez, X.; Błesznowski, M.; Aguado, M.; Niemczyk, A.; Garbayo, I. Techno-economic feasibility of solid oxide electrolysis hybridization with solar photovoltaics and batteries for green hydrogen production. *Energy Convers. Manag. X* **2025**, *27*, 101131. [CrossRef]
7. Ruiz, K.; Judez, X.; Fantova, M.; García-Martín, S.; García-Alvarado, F.; Ciaurriz, P.; Aguado, M.; Garbayo, I. Current market status of solid oxide hydrogen technology: From starting materials to system level. *Energy Rep.* **2026**, *15*, 109091. [CrossRef]
8. Costamagna, P.; Holtappels, P.; Sanna, C. 13-Metal oxide nanofiber-based electrodes in solid oxide fuel cells. In *Metal Oxide-Based Nanofibers and Their Applications*; Esposito, V., Marani, D., Eds.; Elsevier: Amsterdam, The Netherlands, 2022; pp. 301–331.

9. Hanif, M.B.; Rauf, S.; Motola, M.; Babar, Z.U.D.; Li, C.-J.; Li, C.-X. Recent progress of perovskite-based electrolyte materials for solid oxide fuel cells and performance optimizing strategies for energy storage applications. *Mater. Res. Bull.* **2022**, *146*, 111612. [CrossRef]
10. Hou, M.; Pan, Y.; He, F.; Xu, K.; Zhang, H.; Zhou, Y.; Zhao, B.; Chen, Y.; Liu, M. Manipulating and Optimizing the Hierarchically Porous Electrode Structures for Rapid Mass Transport in Solid Oxide Cells. *Adv. Funct. Mater.* **2022**, *32*, 2203722. [CrossRef]
11. Zhao, C.; Li, Y.; Zhang, W.; Zheng, Y.; Lou, X.; Yu, B.; Chen, J.; Chen, Y.; Liu, M.; Wang, J. Heterointerface engineering for enhancing the electrochemical performance of solid oxide cells. *Energy Environ. Sci.* **2020**, *13*, 53–85. [CrossRef]
12. Zhu, K.; Luo, B.; Liu, Z.; Wen, X. Recent advances and prospects of symmetrical solid oxide fuel cells. *Ceram. Int.* **2022**, *48*, 8972–8986. [CrossRef]
13. Mogensen, M.B. Materials for reversible solid oxide cells. *Curr. Opin. Electrochem.* **2020**, *21*, 265–273. [CrossRef]
14. Mahato, N.; Banerjee, A.; Gupta, A.; Omar, S.; Balani, K. Progress in material selection for solid oxide fuel cell technology: A review. *Prog. Mater. Sci.* **2015**, *72*, 141–337. [CrossRef]
15. Jiang, S.P. Development of lanthanum strontium cobalt ferrite perovskite electrodes of solid oxide fuel cells—A review. *Int. J. Hydrogen Energy* **2019**, *44*, 7448–7493. [CrossRef]
16. Sikstrom, D.; Thangadurai, V. A tutorial review on solid oxide fuel cells: Fundamentals, materials, and applications. *Ionics* **2026**, *32*, 5–30. [PubMed]
17. Vairo, T.; Cademartori, D.; Clematis, D.; Asensio, A.M.; Barbucci, A.; Carpanese, M.P. A physics-informed neural network (PINN) predicting the performance of air electrodes for solid oxide cells: A pilot-scale demonstration on four microstructures. *Int. J. Hydrogen Energy* **2025**, *176*, 151322. [CrossRef]
18. Cademartori, D.; Asensio, A.M.; Clematis, D.; Hubert, M.; Laurencin, J.; Barbucci, A. Elucidating the impact of gas transport on high-performing air electrodes: A 1D physically based model unveiling the correlation between microstructure and impedance response. *J. Phys. Energy* **2025**, *7*, 015005.
19. Cademartori, D.; Mercadelli, E.; Gondolini, A.; Asensio, A.M.; Bertei, A.; Sanson, A.; Carpanese, M.P. Fabrication and electrochemical modelling of 8YSZ and GDC10 freeze tape cast scaffolds for solid oxide cells (SOCs). *J. Eur. Ceram. Soc.* **2023**, *43*, 5263–5278. [CrossRef]
20. Majnoni d'Intignano, X.; Cademartori, D.; Clematis, D.; Presto, S.; Viviani, M.; Botter, R.; Barbucci, A.; Cerisola, G.; Caboche, G.; Carpanese, M.P. Infiltrated $Ba_{0.5}Sr_{0.5}Co_{0.8}Fe_{0.2}O_{3-\delta}$-Based Electrodes as Anodes in Solid Oxide Electrolysis Cells. *Energies* **2020**, *13*, 3659. [CrossRef]
21. Di Benedetto, N.; Grassi, J.; Maria Asensio, A.; Kreka, K.; Bernadet, L.; Yedra, L.; Estradé, S.; Peiró, F.; Torrell, M.; Suescun, L.; et al. Cobalt-free compositionally complex nanocomposites with superior performance and stability for application as oxygen electrodes in solid oxide cells. *J. Mater. Chem. A* **2026**, *14*, 11987–12002. [CrossRef]
22. Yang, G.; Zhou, W.; Liu, M.; Shao, Z. Enhancing Electrode Performance by Exsolved Nanoparticles: A Superior Cobalt-Free Perovskite Electrocatalyst for Solid Oxide Fuel Cells. *ACS Appl. Mater. Interfaces* **2016**, *8*, 35308–35314. [CrossRef] [PubMed]
23. Hashim, S.S.; Liang, F.; Zhou, W.; Sunarso, J. Cobalt-Free Perovskite Cathodes for Solid Oxide Fuel Cells. *ChemElectroChem* **2019**, *6*, 3549–3569. [CrossRef]
24. Hussain, M.; Muneer, M.; Abbas, G.; Shakir, I.; Iqbal, A.; Javed, M.A.; Iqbal, M.; Zohaib Ur, R.; Raza, R. Cobalt free LaxSr1-xFe1-yCuyO3-δ (x = 0.54, 0.8, y = 0.2, 0.4) perovskite structured cathode for SOFC. *Ceram. Int.* **2020**, *46*, 18208–18215. [CrossRef]
25. Heywood, S.K.; Romanenko, K.; Sofie, S.W.; Codd, S.L. Intrinsic microstructural anisotropy in tape cast ceramics by ice templating. *Int. J. Appl. Ceram. Technol.* **2020**, *17*, 2202–2211. [CrossRef]
26. Scotti, K.L.; Dunand, D.C. Freeze casting—A review of processing, microstructure and properties via the open data repository, FreezeCasting.net. *Prog. Mater. Sci.* **2018**, *94*, 243–305. [CrossRef]
27. Sofie, S.W. Fabrication of Functionally Graded and Aligned Porosity in Thin Ceramic Substrates With the Novel Freeze–Tape-Casting Process. *J. Am. Ceram. Soc.* **2007**, *90*, 2024–2031. [CrossRef]
28. Buzi, F.; Bernadet, L.; Orrit-Prat, J.; Bonet, R.; Caro, J.; Montinaro, D.; Ouweltjes, J.P.; Baiutti, F.; Torrell, M.; Morata, A.; et al. Advanced manufacturing for efficient GDC diffusion barrier layer by rapid thermal processing for large-area solid oxide cells. *J. Power Sources* **2025**, *652*, 237629. [CrossRef]
29. Bernadet, L.; Buzi, F.; Baiutti, F.; Segura-Ruiz, J.; Dolado, J.; Montinaro, D.; Torrell, M.; Morata, A.; Tarancón, A. Thickness effect of thin-film barrier layers for enhanced long-term operation of solid oxide fuel cells. *APL Energy* **2023**, *1*, 036101. [CrossRef]
30. Wu, S.; Yan, W.; Ni, N.; Zhu, L.; Huang, Z. Densification of ceria-based barrier layer for solid oxide cells at lower sintering temperatures: A review. *J. Adv. Ceram.* **2025**, *14*, 9221001. [CrossRef]
31. Cademartori, D.; Clematis, D. A 2D multi-physics model supporting the interpretation of the dynamic response of button solid oxide cells. *J. Power Sources* **2026**, *684*, 240332. [CrossRef]
32. Cademartori, D.; Trivino-Pelaez, A.; Carpanese, M.P.; Hubert, M.; Laurencin, J. Understanding the microstructure-performance correlations of infiltrated freeze tape cast electrodes for solid oxide cells by physics-based modelling. *Electrochim. Acta* **2025**, *528*, 146187. [CrossRef]

33. Cademartori, D. Unveiling the characteristic EIS fingerprint of the ion-transfer process in air electrodes for solid oxide cells. *J. Electroanal. Chem.* **2025**, *984*, 119026. [CrossRef]
34. Chen, K.; Jiang, S.P. Surface Segregation in Solid Oxide Cell Oxygen Electrodes: Phenomena, Mitigation Strategies and Electrochemical Properties. *Electrochem. Energy Rev.* **2020**, *3*, 730–765. [CrossRef]
35. Skinner, S.J. Recent Advances in the Understanding of the Evolution of Surfaces and Interfaces in Solid Oxide Cells. *Adv. Mater. Interfaces* **2019**, *6*, 1900580. [CrossRef]
36. Effori, E.; Laurencin, J.; Silva, E.D.R.; Hubert, M.; David, T.; Petitjean, M.; Geneste, G.; Dessemond, L.; Siebert, E. An Elementary Kinetic Model for the LSCF and LSCF-CGO Electrodes of Solid Oxide Cells: Impact of Operating Conditions and Degradation on the Electrode Response. *J. Electrochem. Soc.* **2021**, *168*, 044520. [CrossRef]
37. Monaco, F.; Effori, E.; Hubert, M.; Siebert, E.; Geneste, G.; Morel, B.; Djurado, E.; Montinaro, D.; Laurencin, J. Electrode kinetics of porous Ni-3YSZ cermet operated in fuel cell and electrolysis modes for solid oxide cell application. *Electrochim. Acta* **2021**, *389*, 138765. [CrossRef]
38. Shin, H.; Seo, J.; Jeon, S.; Jeong, S.J.; Kim, J.; Lee, S.; Lee, J.J.; Jung, W. Enhanced catalytic activity and stability of SOFC electrodes through plasma-driven surface modification. *J. Mater. Chem. A* **2024**, *12*, 10695–10703. [CrossRef]
39. Ebbesen, S.D.; Sun, X.; Mogensen, M.B. Understanding the processes governing performance and durability of solid oxide electrolysis cells. *Faraday Discuss.* **2015**, *182*, 393–422. [CrossRef] [PubMed]
40. Mogensen, M.B.; Chen, M.; Frandsen, H.L.; Graves, C.; Hansen, J.B.; Hansen, K.V.; Hauch, A.; Jacobsen, T.; Jensen, S.H.; Skafte, T.L.; et al. Reversible solid-oxide cells for clean and sustainable energy. *Clean Energy* **2019**, *3*, 175–201. [CrossRef]
41. Jiang, S.P. Solid-State Electrochemistry and Solid Oxide Fuel Cells: Status and Future Prospects. *Electrochem. Energy Rev.* **2022**, *5*, 21. [CrossRef]
42. Chen, K.; Jiang, S. Review—Materials Degradation of Solid Oxide Electrolysis Cells. *J. Electrochem. Soc.* **2016**, *163*, F3070–F3083. [CrossRef]
43. McPhail, S.J.; Frangini, S.; Laurencin, J.; Effori, E.; Abaza, A.; Padinjarethil, A.K.; Hagen, A.; Léon, A.; Brisse, A.; Vladikova, D.; et al. Addressing planar solid oxide cell degradation mechanisms: A critical review of selected components. *Electrochem. Sci. Adv.* **2022**, *2*, e2100024.
44. Trini, M.; Hauch, A.; De Angelis, S.; Tong, X.; Hendriksen, P.V.; Chen, M. Comparison of microstructural evolution of fuel electrodes in solid oxide fuel cells and electrolysis cells. *J. Power Sources* **2020**, *450*, 227599. [CrossRef]
45. Hubert, M.; Laurencin, J.; Cloetens, P.; Morel, B.; Montinaro, D.; Lefebvre-Joud, F. Impact of Nickel agglomeration on Solid Oxide Cell operated in fuel cell and electrolysis modes. *J. Power Sources* **2018**, *397*, 240–251. [CrossRef]
46. Cademartori, D.; Hubert, M.; Bonnet, E.; Bassat, J.M.; Laurencin, J. Engineering nanostructured electrodes for solid oxide cells (SOCs) via microstructural and electrochemical modelling. *Int. J. Hydrogen Energy* **2025**, *98*, 1396–1414. [CrossRef]
47. Cademartori, D.; Clematis, D.; Carpanese, M.P. Microstructural and electrochemical properties of Ni-impregnated GDC10 and 8YSZ freeze tape cast scaffolds as fuel electrodes for solid oxide cells. *Int. J. Hydrogen Energy* **2024**, *50*, 1050–1063. [CrossRef]
48. Cademartori, D.; Hubert, M.; Cloetens, P.; Carpanese, M.P.; Laurencin, J. The design optimization of nanostructured hierarchical electrodes for solid oxide cells by artificial impregnation. *Mater. Des.* **2024**, *238*, 112663. [CrossRef]
49. Saravanabavan, K.; Cademartori, D.; Hartmann, C.; Hubert, M.; Tochon, P.; Djurado, E.; Laurencin, J. Modelling the electrode performance and numerical optimisation of La2NiO4+δ nanoparticle infiltrated GDC scaffolds for solid oxide cells applications. *Solid State Ion.* **2026**, *443*, 117246. [CrossRef]
50. Davì, R.; Carraro, G.; Stojkovska, M.; Smerieri, M.; Savio, L.; Lewandowski, M.; Gallet, J.-J.; Bournel, F.; Rocca, M.; Vattuone, L. Boudouard reaction under graphene cover on Ni(111). *Appl. Surf. Sci.* **2022**, *599*, 154065. [CrossRef]
51. Carraro, G.; Atakoohi, S.E.; Perilli, D.; Alayan, O.; Bracco, G.; Garbarino, G.; Leidinger, P.M.; Novotny, Z.; Rocca, M.; Savio, L.; et al. Hydrogenation of graphene on Ni(111) by H2 under near ambient pressure conditions. *Mater. Today Chem.* **2024**, *42*, 102359. [CrossRef]
52. Liu, H.; Zakhtser, A.; Naitabdi, A.; Rochet, F.; Bournel, F.; Salzemann, C.; Petit, C.; Gallet, J.-J.; Jie, W. Operando Near-Ambient Pressure X-ray Photoelectron Spectroscopy Study of the CO Oxidation Reaction on the Oxide/Metal Model Catalyst ZnO/Pt(111). *ACS Catal.* **2019**, *9*, 10212–10225. [CrossRef]
53. Novotny, Z.; Aegerter, D.; Comini, N.; Tobler, B.; Artiglia, L.; Maier, U.; Moehl, T.; Fabbri, E.; Huthwelker, T.; Schmidt, T.J.; et al. Probing the solid–liquid interface with tender x rays: A new ambient-pressure x-ray photoelectron spectroscopy endstation at the Swiss Light Source. *Rev. Sci. Instrum.* **2020**, *91*, 023103. [CrossRef] [PubMed]
54. Held, G.; Venturini, F.; Grinter, D.C.; Ferrer, P.; Arrigo, R.; Deacon, L.; Quevedo Garzon, W.; Roy, K.; Large, A.; Stephens, C.; et al. Ambient-pressure endstation of the Versatile Soft X-ray (VerSoX) beamline at Diamond Light Source. *J. Synchrotron Radiat.* **2020**, *27*, 1153–1166. [CrossRef] [PubMed]
55. Sezen, H.; Al-Hada, M.; Amati, M.; Gregoratti, L. In situ chemical and morphological characterization of copper under near ambient reduction and oxidation conditions. *Surf. Interface Anal.* **2018**, *50*, 921–926.

56. Nappini, S.; D'Amario, L.; Favaro, M.; Dal Zilio, S.; Salvador, F.; Betz-Güttner, E.; Fondacaro, A.; Píš, I.; Romanzin, L.; Gambitta, A.; et al. Soft x-ray spectroscopies in liquids and at solid–liquid interface at BACH beamline at Elettra. *Rev. Sci. Instrum.* **2021**, *92*, 015115. [CrossRef] [PubMed]
57. van den Bosch, I.C.G.; Zaman, J.U.; Shterk, G.; Hamed, M.H.; Schneider, M.; Ratovskii, V.; Bu, Y.; Dietrich, P.M.; Koster, G.; Baeumer, C. Laboratory-based in situ and operando tricolor x-ray photoelectron spectroscopy. *Sci. Adv.* **2025**, *11*, eadw6673. [CrossRef] [PubMed]
58. Arble, C.; Jia, M.; Newberg, J.T. Lab-based ambient pressure X-ray photoelectron spectroscopy from past to present. *Surf. Sci. Rep.* **2018**, *73*, 37–57. [CrossRef]
59. Toyoshima, R.; Kondoh, H. In-situ observations of catalytic surface reactions with soft x-rays under working conditions. *J. Phys. Condens. Matter.* **2015**, *27*, 083003. [CrossRef] [PubMed]
60. Zhong, L.; Chen, D.; Zafeiratos, S. A mini review of in situ near-ambient pressure XPS studies on non-noble, late transition metal catalysts. *Catal. Sci. Technol.* **2019**, *9*, 3851–3867. [CrossRef]
61. Nguyen, L.; Tao, F.F.; Tang, Y.; Dou, J.; Bao, X.-J. Understanding Catalyst Surfaces during Catalysis through Near Ambient Pressure X-ray Photoelectron Spectroscopy. *Chem. Rev.* **2019**, *119*, 6822–6905. [CrossRef] [PubMed]
62. Stoerzinger, K.A.; Hong, W.T.; Crumlin, E.J.; Bluhm, H.; Shao-Horn, Y. Insights into electrochemical reactions from ambient pressure photoelectron spectroscopy. *Acc. Chem. Res.* **2015**, *48*, 2976–2983. [CrossRef] [PubMed]
63. Takagi, Y.; Uruga, T.; Tada, M.; Iwasawa, Y.; Yokoyama, T. Ambient Pressure Hard X-ray Photoelectron Spectroscopy for Functional Material Systems as Fuel Cells under Working Conditions. *Acc. Chem. Res.* **2018**, *51*, 719–727. [CrossRef] [PubMed]
64. Amann, P.; Klötzer, B.; Degerman, D.; Köpfle, N.; Götsch, T.; Lömker, P.; Rameshan, C.; Ploner, K.; Bikaljevic, D.; Wang, H.-Y.; et al. The state of zinc in methanol synthesis over a Zn/ZnO/Cu(211) model catalyst. *Science* **2022**, *376*, 603–608. [CrossRef] [PubMed]
65. Goodwin, C.M.; Lömker, P.; Degerman, D.; Davies, B.; Shipilin, M.; Garcia-Martinez, F.; Koroidov, S.; Katja Mathiesen, J.; Rameshan, R.; Rodrigues, G.L.S.; et al. Operando probing of the surface chemistry during the Haber-Bosch process. *Nature* **2024**, *625*, 282–286. [CrossRef] [PubMed]
66. Cai, J.; Gu, Y.; Wang, Z.; Zang, Y.; Lin, S.; Zhang, T.; Han, Y.; Zhang, H.; Wang, Z.-J.; Liu, Z. Laboratory-Based Ambient-Pressure X-ray Photoelectron Spectroscopy for Pressure up to 1 bar. *Photon Sci.* **2025**. [CrossRef]
67. Maibach, J.; Källquist, I.; Andersson, M.; Urpelainen, S.; Edström, K.; Rensmo, H.; Siegbahn, H.; Hahlin, M. Probing a battery electrolyte drop with ambient pressure photoelectron spectroscopy. *Nat. Commun.* **2019**, *10*, 3080. [CrossRef] [PubMed]
68. Wagner, N.; Schnurnberger, W.; Müller, B.; Lang, M. Electrochemical impedance spectra of solid-oxide fuel cells and polymer membrane fuel cells. *Electrochim. Acta* **1998**, *43*, 3785–3793. [CrossRef]
69. Jørgensen, M.J.; Primdahl, S.; Mogensen, M. Characterisation of composite SOFC cathodes using electrochemical impedance spectroscopy. *Electrochim. Acta* **1999**, *44*, 4195–4201. [CrossRef]
70. Klotz, D.; Weber, A.; Ivers-Tiffée, E. Practical Guidelines for Reliable Electrochemical Characterization of Solid Oxide Fuel Cells. *Electrochim. Acta* **2017**, *227*, 110–126. [CrossRef]
71. Costamagna, P.; Sala, E.M.; Zhang, W.; Lund Traulsen, M.; Holtappels, P. Electrochemical impedance spectroscopy of La0.6Sr0.4Co0.2Fe0.8O3-δ nanofiber cathodes for intermediate temperature-solid oxide fuel cell applications: A case study for the 'depressed' or 'fractal' Gerischer element. *Electrochim. Acta* **2019**, *319*, 657–671. [CrossRef]
72. Błaszczak, P.; Mäkinen, P.; Mroziński, A.; Ducka, A.; Jasiński, G.; Himanen, O.; Jasiński, P. Uncovering the electrochemical processes and understanding the causes of the degradation via EIS-DRT in large-scale solid oxide fuel cell. *Appl. Energy* **2025**, *393*, 125983. [CrossRef]
73. Timoshenko, J.; Roldan Cuenya, B. In Situ/Operando Electrocatalyst Characterization by X-ray Absorption Spectroscopy. *Chem. Rev.* **2021**, *121*, 882–961. [PubMed]
74. Amezawa, K. X-ray absorption spectroscopic studies on solid oxide fuel cells and proton-conducting ceramic fuel cells. *Curr. Opin. Electrochem.* **2020**, *21*, 250–256. [CrossRef]
75. Stangl, A.; Muñoz-Rojas, D.; Burriel, M. In situ and operando characterisation techniques for solid oxide electrochemical cells: Recent advances. *J. Phys. Energy* **2021**, *3*, 012001.
76. Kumar, N.; Najimu, M.O.; Cho, Y.J.; Gilliard-AbdulAziz, K.L.; Nikolla, E.; Wu, Z.; Wachs, I.E. Probing Surface/Bulk Structural Chemistry of Key Components of Solid Oxide Electrochemical Cells with In Situ/Operando Raman Spectroscopy. *Chem. Rev.* **2025**, *125*, 8921–8955. [CrossRef] [PubMed]
77. Yu, Y.; Nikiforov, A.Y.; Kaspar, T.C.; Woicik, J.C.; Ludwig, K.F.; Gopalan, S.; Pal, U.B.; Basu, S.N. Chemical characterization of surface precipitates in La0.7Sr0.3Co0.2Fe0.8O3-δ as cathode material for solid oxide fuel cells. *J. Power Sources* **2016**, *333*, 247–253. [CrossRef]
78. Gray, A.X.; Papp, C.; Ueda, S.; Balke, B.; Yamashita, Y.; Plucinski, L.; Minár, J.; Braun, J.; Ylvisaker, E.R.; Schneider, C.M.; et al. Probing bulk electronic structure with hard X-ray angle-resolved photoemission. *Nat. Mater.* **2011**, *10*, 759–764. [CrossRef] [PubMed]

79. Fadley, C.S. Hard X-ray Photoemission: An Overview and Future Perspective. In *Hard X-Ray Photoelectron Spectroscopy (HAXPES)*; Woicik, J., Ed.; Springer International Publishing: Cham, Switzerland, 2016; pp. 1–34.
80. SPECSGROUP. Available online: https://www.specs-group.com/specs/products/detail/nap-xps-system-for-liquid-jets/ (accessed on 12 July 2026).
81. CERIC. Available online: https://www.ceric-eric.eu/lab-instrument/nap-xps/ (accessed on 12 July 2026).
82. Omicron, S. Available online: https://scientaomicron.com/BAR-XPS (accessed on 12 July 2026).
83. Degerman, D.; Amann, P.; Goodwin, C.M.; Lömker, P.; Wang, H.-Y.; Soldemo, M.; Shipilin, M.; Schlueter, C.; Nilsson, A. Operando X-ray Photoelectron Spectroscopy for High-Pressure Catalysis Research Using the POLARIS Endstation. *Synchrotron Radiat. News* **2022**, *35*, 11–18. [CrossRef]
84. Fan, Y.; Wang, X.; Bo, G.; Xu, X.; See, K.W.; Johannessen, B.; Pang, W.K. Operando Synchrotron X-Ray Absorption Spectroscopy: A Key Tool for Cathode Material Studies in Next-Generation Batteries. *Adv. Sci.* **2025**, *12*, 2414480. [CrossRef]
85. BRUKER. Available online: https://www.bruker.com/en/products-and-solutions/raman-spectroscopy/raman-basics/raman-faq.html (accessed on 12 July 2026).
86. Horiba Strain Measurements of a Si Cap Layer Deposited on a SiGe Substrate, Determination of Ge Content. Available online: https://www.horiba.com/int/scientific/applications/semiconductors/pages/strain-measurements-of-a-si-cap-layer-deposited-on-a-sige-substrate-determination-of-ge-content/ (accessed on 13 July 2026).
87. Triviño-Peláez, Á.; Cademartori, D.; Hubert, M.; Rorato, L.; Prioux, M.; Laurencin, J. Modelling the impact of Ni migration and coarsening on the Ni-YSZ electrodes performances based on three-dimensional microstructures. *Electrochim. Acta* **2025**, *520*, 145791. [CrossRef]
88. Monaco, F.; Hubert, M.; Vulliet, J.; Ouweltjes, J.P.; Montinaro, D.; Cloetens, P.; Piccardo, P.; Lefebvre-Joud, F.; Laurencin, J. Degradation of Ni-YSZ Electrodes in Solid Oxide Cells: Impact of Polarization and Initial Microstructure on the Ni Evolution. *J. Electrochem. Soc.* **2019**, *166*, F1229. [CrossRef]
89. Porotnikova, N.; Osinkin, D. Segregation and interdiffusion processes in perovskites: A review of recent advances. *J. Mater. Chem. A* **2024**, *12*, 2620–2646. [CrossRef]
90. Dang, X.; Lu, Y.; Fan, Z.; Jiang, Y.; Gao, Z. Strategies to mitigate Sr segregation of the LSCF oxygen electrode for solid oxide cells. *J. Mater. Chem. A* **2025**, *13*, 20268–20288. [CrossRef]
91. Navasa, M.; Frandsen, H.L.; Skafte, T.L.; Sundén, B.; Graves, C. Localized carbon deposition in solid oxide electrolysis cells studied by multiphysics modeling. *J. Power Sources* **2018**, *394*, 102–113. [CrossRef]
92. Tao, Y.; Ebbesen, S.D.; Mogensen, M.B. Carbon Deposition in Solid Oxide Cells during Co-Electrolysis of H_2O and CO_2. *J. Electrochem. Soc.* **2014**, *161*, F337. [CrossRef]
93. DeCaluwe, S.C.; Grass, M.E.; Zhang, C.; Gabaly, F.E.; Bluhm, H.; Liu, Z.; Jackson, G.S.; McDaniel, A.H.; McCarty, K.F.; Farrow, R.L.; et al. In Situ Characterization of Ceria Oxidation States in High-Temperature Electrochemical Cells with Ambient Pressure XPS. *J. Phys. Chem. C* **2010**, *114*, 19853–19861. [CrossRef]
94. Zhang, C.; Grass, M.E.; Yu, Y.; Gaskell, K.J.; DeCaluwe, S.C.; Chang, R.; Jackson, G.S.; Hussain, Z.; Bluhm, H.; Eichhorn, B.W.; et al. Multielement Activity Mapping and Potential Mapping in Solid Oxide Electrochemical Cells through the use of operando XPS. *ACS Catal.* **2012**, *2*, 2297–2304. [CrossRef]
95. Zhang, C.; Grass, M.E.; McDaniel, A.H.; DeCaluwe, S.C.; El Gabaly, F.; Liu, Z.; McCarty, K.F.; Farrow, R.L.; Linne, M.A.; Hussain, Z.; et al. Measuring fundamental properties in operating solid oxide electrochemical cells by using in situ X-ray photoelectron spectroscopy. *Nat. Mater.* **2010**, *9*, 944–949. [CrossRef] [PubMed]
96. Nurk, G.; Kooser, K.; Urpelainen, S.; Käämbre, T.; Joost, U.; Kodu, M.; Kivi, I.; Kanarbik, R.; Kukk, E.; Lust, E. Near ambient pressure X-ray photoelectron-and impedance spectroscopy study of NiO-Ce0.9Gd0.1O2-δ anode reduction using a novel dual-chamber spectroelectrochemical cell. *J. Power Sources* **2018**, *378*, 589–596. [CrossRef]
97. Nurk, G.; Kooser, K.; Korjus, O.; Kanarbik, R.; Urpelainen, S.; Käämbre, T.; Joost, U.; Kook, M.; Kodu, M.; Möller, P.; et al. Operando NAP-HT-XPS and Impedance Spectroscopy Study of Pulsed Laser Deposited Ni-$Ce_{0.9}Gd_{0.1}O_{2-\delta}$ Solid Oxide Fuel Cell Electrode. *ECS Trans.* **2019**, *91*, 555. [CrossRef]
98. Paloukis, F.; Papazisi, K.M.; Dintzer, T.; Papaefthimiou, V.; Saveleva, V.A.; Balomenou, S.P.; Tsiplakides, D.; Bournel, F.; Gallet, J.-J.; Zafeiratos, S. Insights into the Surface Reactivity of Cermet and Perovskite Electrodes in Oxidizing, Reducing, and Humid Environments. *ACS Appl. Mater. Interfaces* **2017**, *9*, 25265–25277. [CrossRef] [PubMed]
99. Zhang, J.; Barreau, M.; Dintzer, T.; Haevecker, M.; Teschner, D.; Efimenko, A.; Luo, W.; Zafeiratos, S. Unveiling Key Interface Characteristics of Ni/Yttria-Stabilized Zirconia Solid Oxide Cell Electrodes in H2O Electroreduction Using Operando X-ray Photoelectron Spectroscopy. *ACS Appl. Mater. Interfaces* **2024**, *16*, 37915–37926. [CrossRef] [PubMed]
100. Bozzini, B.; Amati, M.; Mele, C.; Knop-Gericke, A.; Vesselli, E. An in situ near-ambient pressure X-ray photoelectron spectroscopy study of CO_2 reduction at Cu in a SOE cell. *J. Electroanal. Chem.* **2017**, *799*, 17–25. [CrossRef]

101. Bozzini, B.; Amati, M.; Bocchetta, P.; Dal Zilio, S.; Knop-Gericke, A.; Vesselli, E.; Kiskinova, M. An in situ near-ambient pressure X-ray Photoelectron Spectroscopy study of Mn polarised anodically in a cell with solid oxide electrolyte. *Electrochim. Acta* **2015**, *174*, 532–541. [CrossRef]
102. Nurk, G.; Ainsar, M.; Kodu, M.; Kelp, G.; Romann, T.; Lust, E.; Gallet, J.-J.; Kukk, E.; Kooser, K.; Möller, P. Electrochemical Activation and NAP-XPS As Well As EIS Characterization of $La_{0.31}Sr_{0.58}Ti_{0.97}Ni_{0.03}O_{3-\delta}$ Thin Film Electrode. *ECS Trans.* **2023**, *111*, 579. [CrossRef]
103. Ainsar, M.; Kooser, K.; Kodu, M.; Kelp, G.; Tamm, A.; Käämbre, T.; Möller, P.; Romann, T.; Hävecker, M.; Götsch, T.; et al. In situ NAP-XPS and electrochemical impedance characterisation of $La_{0.31}Sr_{0.58}Ti_{0.97}Ni_{0.03}O_{3-\delta}$ thin film model electrodes. *J. Power Sources* **2025**, *651*, 237457. [CrossRef]
104. Rowberg, A.J.E.; Slomski, H.S.; Kim, N.; Strange, N.A.; Gorman, B.P.; Shulda, S.; Ginley, D.S.; Kweon, K.E.; Wood, B.C. Impact of Sr-Containing Secondary Phases on Oxide Conductivity in Solid-Oxide Electrolyzer Cells. *Chem. Mater.* **2024**, *36*, 6464–6474. [CrossRef]
105. Crumlin, E.J.; Mutoro, E.; Liu, Z.; Grass, M.E.; Biegalski, M.D.; Lee, Y.-L.; Morgan, D.; Christen, H.M.; Bluhm, H.; Shao-Horn, Y. Surface strontium enrichment on highly active perovskites for oxygen electrocatalysis in solid oxide fuel cells. *Energy Environ. Sci.* **2012**, *5*, 6081–6088. [CrossRef]
106. Bozzini, B.; Previdi, A.; Amati, M.; Bevilacqua, M.; Cordaro, G.; Corva, M.; Donazzi, A.; Dotelli, G.; Gregoratti, L.; Pelosato, R.; et al. In situ near-ambient pressure X-ray photoelectron spectroscopy discloses the surface composition of operating $NdBaCo_2O_{5+\delta}$ solid oxide fuel cell cathodes. *J. Power Sources* **2019**, *436*, 226815. [CrossRef]
107. Hong, W.T.; Stoerzinger, K.A.; Crumlin, E.J.; Mutoro, E.; Jeen, H.; Lee, H.N.; Shao-Horn, Y. Near-Ambient Pressure XPS of High-Temperature Surface Chemistry in $Sr_2Co_2O_5$ Thin Films. *Top. Catal.* **2016**, *59*, 574–582. [CrossRef]
108. Nenning, A.; Opitz, A.K.; Rameshan, C.; Rameshan, R.; Blume, R.; Hävecker, M.; Knop-Gericke, A.; Rupprechter, G.; Klötzer, B.; Fleig, J. Ambient Pressure XPS Study of Mixed Conducting Perovskite-Type SOFC Cathode and Anode Materials under Well-Defined Electrochemical Polarization. *J. Phys. Chem. C* **2016**, *120*, 1461–1471. [CrossRef]
109. Chen, Y.; Chen, Y.; Ding, D.; Ding, Y.; Choi, Y.; Zhang, L.; Yoo, S.; Chen, D.; deGlee, B.; Xu, H.; et al. A robust and active hybrid catalyst for facile oxygen reduction in solid oxide fuel cells. *Energy Environ. Sci.* **2017**, *10*, 964–971. [CrossRef]
110. Opitz, A.K.; Rameshan, C.; Kubicek, M.; Rupp, G.M.; Nenning, A.; Götsch, T.; Blume, R.; Hävecker, M.; Knop-Gericke, A.; Rupprechter, G.; et al. The Chemical Evolution of the $La_{0.6}Sr_{0.4}CoO_{3-\delta}$ Surface Under SOFC Operating Conditions and Its Implications for Electrochemical Oxygen Exchange Activity. *Top. Catal.* **2018**, *61*, 2129–2141. [CrossRef] [PubMed]
111. Rameshan, R.; Nenning, A.; Raschhofer, J.; Lindenthal, L.; Ruh, T.; Summerer, H.; Opitz, A.K.; Martin Huber, T.; Rameshan, C. Novel Sample-Stage for Combined Near Ambient Pressure X-ray Photoelectron Spectroscopy, Catalytic Characterization and Electrochemical Impedance Spectroscopy. *Crystals* **2020**, *10*, 947. [CrossRef]
112. Thurner, C.W.; Haug, L.; Winkler, D.; Zarth, V.; Glätzle, J.; Ploner, K.; Schäfer, J.; Penner, S.; Klötzer, B. Preparation of Ni and NiCu/Yttria-Stabilized Zirconia Model Electrodes with Optimized Triple-Phase Boundary Geometry for Fundamental Operando Spectroscopic Studies. *Small Struct.* **2024**, *5*, 2300414.
113. Chen, D.; Barreau, M.; Dintzer, T.; Turczyniak-Surdacka, S.; Bournel, F.; Gallet, J.-J.; Zafeiratos, S. Surface oxidation of Ni-cermet electrodes by CO_2 and H_2O and how to moderate it. *J. Energy Chem.* **2022**, *67*, 300–308. [CrossRef]
114. Chen, D.; Barreau, M.; Turczyniak-Surdacka, S.; Sobczak, K.; Strawski, M.; Salle, A.L.G.L.; Efimenko, A.; Teschner, D.; Petit, C.; Zafeiratos, S. Ceria nanoparticles as promoters of CO_2 electroreduction on Ni/YSZ: An efficient preparation strategy and insights into the catalytic promotion mechanism. *Nano Energy* **2022**, *101*, 107564. [CrossRef]
115. Radtke, M.; Kopp, K.; Hess, C. Coupling Long-Range Raman with X-Ray Photoelectron Spectroscopy for Complementary Bulk and Surface Characterization of Battery Materials. *Chemistry–Methods* **2022**, *2*, e202100058. [CrossRef]
116. Sirotina, A.P.; Callaert, C.; Volykhov, A.A.; Frolov, A.S.; Sánchez-Barriga, J.; Knop-Gericke, A.; Hadermann, J.; Yashina, L.V. Mechanistic Studies of Gas Reactions with Multicomponent Solids: What Can We Learn By Combining NAP XPS and Atomic Resolution STEM/EDX? *J. Phys. Chem. C* **2019**, *123*, 26201–26210. [CrossRef]